



HAL
open science

A bi-projection method for Bingham type flows

Laurent Chupin, Thierry Dubois

► **To cite this version:**

Laurent Chupin, Thierry Dubois. A bi-projection method for Bingham type flows. *Computers & Mathematics with Applications*, 2016, 72 (5), pp.1263-1286. 10.1016/j.camwa.2016.06.026 . hal-01166406v2

HAL Id: hal-01166406

<https://hal.science/hal-01166406v2>

Submitted on 2 Mar 2016

HAL is a multi-disciplinary open access archive for the deposit and dissemination of scientific research documents, whether they are published or not. The documents may come from teaching and research institutions in France or abroad, or from public or private research centers.

L'archive ouverte pluridisciplinaire **HAL**, est destinée au dépôt et à la diffusion de documents scientifiques de niveau recherche, publiés ou non, émanant des établissements d'enseignement et de recherche français ou étrangers, des laboratoires publics ou privés.

A BI-PROJECTION METHOD FOR BINGHAM TYPE FLOWS

LAURENT CHUPIN AND THIERRY DUBOIS

ABSTRACT. We propose and study a new numerical scheme to compute the isothermal and unsteady flow of an incompressible viscoplastic Bingham medium. The main difficulty, for both theoretical and numerical approaches, is due to the non-differentiability of the plastic part of stress tensor in regions where the rate-of-strain tensor vanishes. This is handled by reformulating the definition of the plastic stress tensor in terms of a projection. A new time scheme, based on the classical incremental projection method for the Newtonian Navier-Stokes equations, is proposed. The plastic tensor is treated implicitly in the first sub-step of the projection scheme and is computed by using a fixed point procedure. A pseudo-time relaxation is added into the Bingham projection whose effect is to ensure a geometric convergence of the fixed point algorithm. This is a key feature of the bi-projection scheme which provides a fast and accurate computation of the plastic tensor. Stability and error analyses of the numerical scheme are provided. The error induced by the pseudo-time relaxation term is controlled by a prescribed numerical parameter so that a first-order estimate of the time error is derived for the velocity field. A second-order cell-centred finite volume scheme on staggered grids is applied for the spatial discretisation. The scheme is assessed against previously published benchmark results for both Newtonian and Bingham flows in a two-dimensional lid-driven cavity for Reynolds number equals 1 000. Moreover, the proposed numerical scheme is able to reproduce the fundamental property of cessation in finite time of a viscoplastic medium in the absence of any energy source term in the equations. For a fixed value (100) of the Bingham number, various numerical simulations for a range of Reynolds numbers up to 200 000 were performed with the bi-projection scheme on a grid with 1024^2 mesh points. The effect of this (physical) parameter on the flow behaviour is discussed.

76D05 and 76A05 and 65M12 and 76M12 and 65Y05

1. INTRODUCTION

Many materials occurring in industrial or geophysical problems, such as pastes or polymer suspensions, mud used in drilling technologies, lava, even blood in arterioles and capillaries, behave as viscous fluid flows in regions of high shear stress and as rigid bodies where the stress is below a critical value, called the yield stress. A typical situation found in engineering context is the solidification of flows of a viscoplastic medium in pipes. An important property of these non-Newtonian materials is that the flow returns to rest in a finite time in the absence of any energy source terms. The model which takes into account such viscoplastic behaviour is known as the Bingham model and corresponds to the momentum conservation law for which the stress has a singularity. More precisely, when the shear strain rate magnitude vanishes, the shear stress is not prescribed.

This singularity is a permanent source of challenging problems both from the theoretical point of view and in the design of efficient numerical algorithms capable to produce reliable and accurate numerical simulations. In order to handle this non-differentiability of the constitutive rheological law, two approaches have been mainly used both in the fields of theoretical studies

Date: March 2, 2016.

and numerical simulations. The first one consists in approximating the Bingham model by a *smooth* (differentiable) functional, see for instance [3] or [20]. Such regularising methods are appealing as they can be easily incorporated in classical numerical schemes and implemented in many existing codes designed for the numerical simulation of flows of quasi-Newtonian viscous fluids. They have been widely used to perform numerical simulations of flows of an incompressible Bingham medium, see for instance [3], [15], [5] and [25]. However, a main drawback of the regularisation approach is that, unlike in the original model, yield zones are not clearly defined. Indeed, the regularised model considers the whole flow as a fluid with a spatially variable viscosity so that there is not anymore a clear separation between regions where the material behaves like a fluid or like a solid. Also, as it is mentioned in [5], regularisation methods do not accurately reproduce the cessation of Bingham fluid flows in finite time. Let us finally mention that Zhang in [28] performed a numerical analysis of a regularised Bingham model, used in [3], and derived both time and spatial error bounds for a fully discrete system of equations.

The second approach, used to overcome the difficulty due to the non-differentiable form of the constitutive law, relies on the theory of variational inequalities due to Duvaut and Lions [9]. In this context the Bingham equations can be interpreted with Lagrange multipliers so that the problem reduces in solving several saddle-point problems. These minimisation problems are generally solved by using the Augmented Lagrangian method [10] or the Uzawa-like method [11]. A review of numerical schemes based on this approach can be found in [7]. The variational inequality formulation is particularly well suited for finite element approximations. Therefore, these methods have been mostly used in this context for the spatial discretisation of the equations [7, 27, 21]. Numerical schemes based on the finite difference method have been more recently proposed and used. Two types of schemes have been employed whose main difference rely in the choice of the locations of the discrete variables on the computational grid, namely staggered in [17, 16] and semi-staggered in [19, 18].

Regarding the time discretisation of the (non-regularised) Bingham problem, operator splitting methods are commonly used (see [22, 6, 27]). Most contributions in this context use three sub-steps for the computation of the velocity field per each time iteration. They decouple the resolution of the Stokes operator, that is the viscous term including the incompressibility constraint, of the nonlinear transport terms and of the plastic Bingham contribution. Obviously, the main advantage with such approach is to separate and isolate the difficulties so that efficient and well-known numerical schemes can be applied for solving each sub-steps.

Projection methods are widely used for the time discretisation of the incompressible Navier-stokes equations [12] especially for the numerical simulation of turbulent flows. Indeed, coupling a projection scheme with a cell-centred finite difference or finite volume scheme for the nonlinear terms on staggered grids allows to recover at the discrete level the fundamental orthogonality property (with respect to the L^2 -inner product and its discrete counterpart) of the nonlinear terms with the divergence-free velocity field. This ensures conservation of the kinetic energy for inviscid flows. Surprisingly, projection schemes have not been used in numerical studies of Bingham flows until recently. Indeed, Muravleva in [16] proposed a three-level splitting scheme consisting of a second-order (BDF2) projection scheme for the first two steps followed by a plasticity step, computing the plastic part of the stress tensor with an Uzawa-like method. Sequences of velocity fields and tensors provided by this iterative fixed point procedure both converge. However, from the best of our knowledge, no estimate of the convergence rate has been derived so far.

In this paper, we introduce a new time discretisation scheme to solve the Bingham problem. The main idea is to couple a first-order incremental projection scheme with a projection formulation for the definition of the plastic tensor, which overcomes the difficulty due to the non-differentiable form of the original definition. Unlike in [16], the plastic stress tensor is directly incorporated into the prediction step of the projection scheme and is treated implicitly. As in the Uzawa-like method, a fixed-point algorithm aims to solve the Bingham projection. In order to improve the convergence of this iterative procedure, a pseudo-time relaxation term is added in the computation of the plastic tensor through the Bingham projection. With this modification, the fixed point algorithm now has a geometric convergence and its common ratio depends on a (prescribed) numerical parameter. We therefore obtain a reasonably fast method to compute the plastic part of the stress tensor. Note also that no specific programming skills are required to implement this iterative Bingham projection in any Newtonian flow solver based on a time projection scheme. The objective of this paper is first to perform numerical analyses (stability study and error analysis) of the proposed time scheme and to show the capability of these new methodologies to perform numerical simulations on classical and well-known computational flow configurations at large Bingham and Reynolds numbers.

The outline of the rest of the paper is as follows. In section 2 we precisely provide the mathematical formulation, and the notations, for a Bingham model. We also introduce a definition of the plastic part of the stress tensor based on a projection formulation, which will be used in the next parts. In section 3, the bi-projection time scheme, whose aim is to approximate the continuous model, is described. In this section, we also prove that this method is well posed, stable and convergent. Moreover, the bi-projection scheme is shown to be first-order in time. Indeed, the additional pseudo-time relaxation term induces a perturbation error which can be estimated and controlled so that the bi-projection scheme is first-order accurate with respect to the time discretisation. Finally, in section 4, we first describe in details the spatial discretisation used for the numerical simulations. Then, using a regularised lid-driven cavity as computational configuration, simulations are performed in order to validate the numerical solver: the theoretical convergence rates are recovered. The bi-projection scheme is also shown to be able to reproduce the characteristic property of Bingham flows to return to rest in finite time after forcing terms are removed. Numerical simulations of flows in a two-dimensional lid-driven cavity for Reynolds number equals 1000 and for various Bingham numbers (up to 100) are compared to previously published benchmark results. As it is built on the original model, the proposed scheme accurately predicts unyielded zones. Finally, numerical simulations for Bingham number set to 100 and for a wide range of Reynolds numbers (up to 200 000) are presented. This demonstrates the ability of the bi-projection scheme to handle large Bingham and Reynolds numbers.

2. THE MODEL OF A BINGHAM VISCOUS PLASTIC FLOW

2.1. Mathematical modelling. Let $T > 0$ be a positive real number and Ω be a bounded domain of \mathbb{R}^d . The isothermal flow of an incompressible Bingham viscoplastic medium is modelled by the following system of equations on the velocity \mathbf{u} and the pressure p :

$$(1) \quad \begin{cases} \rho_0(\partial_t \mathbf{u} + \mathbf{u} \cdot \nabla \mathbf{u}) + \nabla p = \operatorname{div} \boldsymbol{\tau} & \text{in } (0, T) \times \Omega, \\ \operatorname{div} \mathbf{u} = 0 & \text{in } (0, T) \times \Omega, \end{cases}$$

where the stress deviator tensor $\boldsymbol{\tau}$ is given with respect to strain rate tensor $\mathbf{D}\mathbf{u} = \frac{1}{2}(\nabla\mathbf{u} + {}^T(\nabla\mathbf{u}))$ by the relation

$$(2) \quad \boldsymbol{\tau} = 2\mu_0 \mathbf{D}\mathbf{u} + \sigma_0 \frac{\mathbf{D}\mathbf{u}}{|\mathbf{D}\mathbf{u}|}.$$

In the equations (1)–(2), the constant ρ_0 represents the density of the medium, the constant μ_0 corresponds to its viscosity and the constant σ_0 is the plasticity yield¹. The notation $|\mathbf{D}\mathbf{u}|$ represents the Froebenius norm of the rate-of-strain tensor:

$$|\mathbf{D}\mathbf{u}| = \left(\sum_{1 \leq i, j \leq d} |(\mathbf{D}\mathbf{u})_{ij}|^2 \right)^{1/2}.$$

Finally the system is supplemented with an initial condition ($\mathbf{u} = \mathbf{u}_{\text{init}}$ for $t = 0$) and boundary conditions ($\mathbf{u} = \mathbf{u}_b$ on $\partial\Omega$). For the sake of simplicity and only for the theoretical analysis of the numerical scheme, we shall consider only homogeneous Dirichlet boundary conditions, namely: $\mathbf{u}_b = \mathbf{0}$. We point out that the results derived in the following sections remain true for the case of non-homogeneous boundary conditions as long as \mathbf{u}_b is tangent to the boundary.

When $\sigma_0 > 0$, the above model makes no sense on the rigid set, that is in the sub-domain of $\Omega \times (0, T)$ where the strain rate tensor vanishes. In order to remedy this lack of definition, the constitutive equation (2) can be written as (see [21] for instance)

$$\boldsymbol{\tau} = 2\mu_0 \mathbf{D}\mathbf{u} + \sigma_0 \boldsymbol{\sigma},$$

where the extra-stress tensor $\boldsymbol{\sigma}$ satisfies

$$(3) \quad \begin{cases} \boldsymbol{\sigma} = \frac{\mathbf{D}\mathbf{u}}{|\mathbf{D}\mathbf{u}|} & \text{if } |\mathbf{D}\mathbf{u}| \neq 0, \\ |\boldsymbol{\sigma}| \leq 1, \quad {}^T\boldsymbol{\sigma} = \boldsymbol{\sigma}, \quad \text{tr } \boldsymbol{\sigma} = 0 & \text{if } |\mathbf{D}\mathbf{u}| = 0. \end{cases}$$

By definition, the deviatoric part of the stress tensor is trace free and so is the extra (plastic) tensor $\boldsymbol{\sigma}$. From (3), this property is obviously satisfied when $|\mathbf{D}\mathbf{u}| \neq 0$.

2.2. A projection formulation. As it is shown in the following proposition, the definition of the tensor $\boldsymbol{\sigma}$ given by (3) can be reformulated in terms of a projection. Such formulation is convenient and is often used in the derivation of iterative methods of Uzawa types for the numerical approximation of $\boldsymbol{\sigma}$ (see [7] and [16] for instance).

Proposition 1. *For all $r > 0$, the condition (3) is equivalent to the relation*

$$(4) \quad \boldsymbol{\sigma} = \mathbb{P}(\boldsymbol{\sigma} + r \mathbf{D}\mathbf{u}),$$

where \mathbb{P} is the projection operator on the closed convex set defined by

$$\Lambda := \left\{ \boldsymbol{\lambda} \in L^2(\Omega)^{d \times d} ; {}^T\boldsymbol{\lambda} = \boldsymbol{\lambda}, \text{tr } \boldsymbol{\lambda} = 0, |\boldsymbol{\lambda}(\mathbf{x})| \leq 1 \text{ for almost all } x \in \Omega \right\}.$$

Proof. If $|\mathbf{D}\mathbf{u}| = 0$ the equivalence is obvious as we have in both cases $\boldsymbol{\sigma} \in \Lambda$.

¹Note that in some papers (for instance [7]), the plasticity yield is $\sqrt{2}\sigma_0$.

Let us now assume that $|\mathbf{Du}| \neq 0$. Note that, for all $\boldsymbol{\lambda} \in L^2(\Omega)^{d \times d}$, such that ${}^T \boldsymbol{\lambda} = \boldsymbol{\lambda}$ and $\text{tr } \boldsymbol{\lambda} = 0$, an explicit expression of its projection $\mathbb{P}(\boldsymbol{\lambda})$ onto Λ is given by (almost everywhere on Ω):

$$(5) \quad \mathbb{P}(\boldsymbol{\lambda}) = \begin{cases} \boldsymbol{\lambda} & \text{if } |\boldsymbol{\lambda}| \leq 1, \\ \boldsymbol{\lambda}/|\boldsymbol{\lambda}| & \text{if } |\boldsymbol{\lambda}| > 1. \end{cases}$$

Consequently, by taking $\boldsymbol{\sigma} = \frac{\mathbf{Du}}{|\mathbf{Du}|}$, which is trace-less and symmetric, we can write for any $r > 0$, $\boldsymbol{\sigma} + r \mathbf{Du} = (1 + r|\mathbf{Du}|) \frac{\mathbf{Du}}{|\mathbf{Du}|}$ so that, according to (5), we have

$$\mathbb{P}(\boldsymbol{\sigma} + r \mathbf{Du}) = \frac{\mathbf{Du}}{|\mathbf{Du}|},$$

and hence $\mathbb{P}(\boldsymbol{\sigma} + r \mathbf{Du}) = \boldsymbol{\sigma}$.

Reciprocally, if $\boldsymbol{\sigma} = \mathbb{P}(\boldsymbol{\sigma} + r \mathbf{Du})$ then $|\boldsymbol{\sigma} + r \mathbf{Du}| > 1$ (otherwise, using (5) we would have $\mathbf{Du} = \mathbf{0}$). Consequently, we have

$$\boldsymbol{\sigma} = \frac{\boldsymbol{\sigma} + r \mathbf{Du}}{|\boldsymbol{\sigma} + r \mathbf{Du}|}.$$

The above equality, implying in particular that $|\boldsymbol{\sigma}| = 1$, can be rewritten as

$$\boldsymbol{\sigma} = \frac{r}{|\boldsymbol{\sigma} + r \mathbf{Du}| - 1} \mathbf{Du}.$$

It follows easily that $\boldsymbol{\sigma} = \frac{\mathbf{Du}}{|\mathbf{Du}|}$. □

Remark 1.

✓ *Instead of working with the Bingham model (1)–(2), a classical approach consists in introducing a small parameter ε and regularising the constitutive relation (2) by writing, see [3] for instance,*

$$\boldsymbol{\tau} = 2\mu_0 \mathbf{Du} + \sigma_0 \frac{\mathbf{Du}}{\sqrt{|\mathbf{Du}|^2 + \varepsilon^2}}.$$

Note that other regularised forms can be used (see [14] for a review). This approach has many advantages from a theoretical point of view. One can relatively easily show the existence of a solution $(\mathbf{u}_\varepsilon, p_\varepsilon)$ for each value of $\varepsilon > 0$. Passing to the limit $\varepsilon \rightarrow 0$, the existence of a solution (\mathbf{u}, p) to the original problem (1)–(2) can be obtained. Nevertheless, from a numerical point of view the behaviour of $(\mathbf{u}_\varepsilon, p_\varepsilon)$, even for small values of ε , can be quite different from the desired behaviour. For instance, without source term (that is without external volume force as in (1) and with $\mathbf{u}_b = \mathbf{0}$) the well-known property that $\mathbf{u}(t) \rightarrow 0$ in finite time is lost.

2.3. A non-dimensional form of the Bingham model. In order to write the system in dimensionless form we introduce a characteristic length L and a characteristic velocity V . Consequently, a natural characteristic time is given by L/V and a characteristic pressure by $\rho_0 V^2$. By scaling all variables with respect to these characteristic quantities, the model of a Bingham viscous plastic flow reads in dimensionless form

$$(6) \quad \partial_t \mathbf{u} + \mathbf{u} \cdot \nabla \mathbf{u} + \nabla p - \frac{1}{\Re e} \Delta \mathbf{u} = \frac{\mathfrak{Bi}}{\Re e} \text{div } \boldsymbol{\sigma},$$

under the conditions (r being any positive parameter)

$$(7) \quad \operatorname{div} \mathbf{u} = 0 \quad \text{and} \quad \boldsymbol{\sigma} = \mathbb{P}(\boldsymbol{\sigma} + r \mathbf{D}\mathbf{u}),$$

where the dimensionless Reynolds and Bingham numbers are respectively defined as

$$\Re = \frac{\rho_0 V L}{\mu_0} \quad \text{and} \quad \mathfrak{B}i = \frac{\sigma_0 L}{\mu_0 V}.$$

3. ANALYSIS OF A FIRST-ORDER BI-PROJECTION SCHEME

3.1. Time discretisation. In this section, we propose a new scheme to discretise with respect to the time variable the Stokes-Bingham equations, namely the equations (6)–(7) where the convective term $\mathbf{u} \cdot \nabla \mathbf{u}$ is omitted:

$$(8) \quad \begin{cases} \partial_t \mathbf{u} + \nabla p - \frac{1}{\Re} \Delta \mathbf{u} = \frac{\mathfrak{B}i}{\Re} \operatorname{div} \boldsymbol{\sigma}, \\ \operatorname{div} \mathbf{u} = 0, \\ \boldsymbol{\sigma} = \mathbb{P}(\boldsymbol{\sigma} + r \mathbf{D}\mathbf{u}). \end{cases}$$

Remark 2. *In practice, the nonlinear term $\mathbf{u} \cdot \nabla \mathbf{u}$ will be taken into account when performing numerical simulations (see the section 4). However, in order to avoid unnecessary technical difficulties (see [23, 24]), we present hereafter a convergence and error analysis only in the linear (Stokes) case. Indeed, the essential difficulty here relies on the coupling of a projection scheme for the Stokes operator and the projection (4) of the yield stress tensor.*

In order to solve (8) we advocate the fixed point algorithm below in which we introduce four numerical parameters (δt , r , α and θ):

We start with $\mathbf{u}^0 = \mathbf{u}_{\text{init}}$ and with arbitrary $\boldsymbol{\sigma}^0$ and p^0 .

For $n \geq 0$, assuming that \mathbf{u}^n , $\boldsymbol{\sigma}^n$ and p^n are known, $(\tilde{\mathbf{u}}^{n+1}, \boldsymbol{\sigma}^{n+1})$ are computed by solving

$$(9) \quad \begin{cases} \frac{\tilde{\mathbf{u}}^{n+1} - \mathbf{u}^n}{\delta t} + \nabla p^n - \frac{1}{\Re} \Delta \tilde{\mathbf{u}}^{n+1} = \frac{\mathfrak{B}i}{\Re} \operatorname{div} \boldsymbol{\sigma}^{n+1}, \\ \boldsymbol{\sigma}^{n+1} = \mathbb{P}(\boldsymbol{\sigma}^{n+1} + r \mathbf{D}\tilde{\mathbf{u}}^{n+1} + \theta(\boldsymbol{\sigma}^n - \boldsymbol{\sigma}^{n+1})), \\ \tilde{\mathbf{u}}^{n+1} \Big|_{\partial\Omega} = \mathbf{0}. \end{cases}$$

Note that, the predicted velocity field $\tilde{\mathbf{u}}^{n+1}$ being non-solenoidal, the symmetric tensor $\boldsymbol{\sigma}^{n+1} + r \mathbf{D}\tilde{\mathbf{u}}^{n+1} + \theta(\boldsymbol{\sigma}^n - \boldsymbol{\sigma}^{n+1})$ is not trace-less. Nevertheless, the explicit formulae (5) can still be used in practice to compute $\boldsymbol{\sigma}^{n+1}$, as we have $\mathbb{P}(\boldsymbol{\lambda}) = \mathbb{P}(\boldsymbol{\lambda} - \frac{1}{d} \operatorname{tr} \boldsymbol{\lambda})$ for any symmetric tensor $\boldsymbol{\lambda}$.

Next, $(\mathbf{u}^{n+1}, p^{n+1})$ are computed by imposing the free-divergence constraint:

$$(10) \quad \begin{cases} \frac{\mathbf{u}^{n+1} - \tilde{\mathbf{u}}^{n+1}}{\delta t} + \alpha \nabla (p^{n+1} - p^n) = \mathbf{0}, \\ \operatorname{div} \mathbf{u}^{n+1} = 0, \\ \mathbf{u}^{n+1} \cdot \mathbf{n} \Big|_{\partial\Omega} = 0. \end{cases}$$

We will prove in the next section that the sequence $(\mathbf{u}^n)_n$ converges to the solution \mathbf{u} of the system (8) (see Theorem 3).

In practice, in order to solve the system (9) we use a sub-fixed-point procedure. We set $\boldsymbol{\sigma}^{n,0} = \boldsymbol{\sigma}^n$. For $k \geq 0$, by assuming that $\boldsymbol{\sigma}^{n,k}$ is known, we define $\tilde{\mathbf{u}}^{n,k}$ as the solution of the following Laplace type problem

$$(11) \quad \begin{cases} \frac{\tilde{\mathbf{u}}^{n,k} - \mathbf{u}^n}{\delta t} + \nabla p^n - \frac{1}{\Re e} \Delta \tilde{\mathbf{u}}^{n,k} = \frac{\Im i}{\Re e} \operatorname{div} \boldsymbol{\sigma}^{n,k}, \\ \tilde{\mathbf{u}}^{n,k} \Big|_{\partial\Omega} = \mathbf{0}. \end{cases}$$

Then, a projection is used to deduce the extra-stress tensor $\boldsymbol{\sigma}^{n,k+1}$, namely:

$$(12) \quad \boldsymbol{\sigma}^{n,k+1} = \mathbb{P}(\boldsymbol{\sigma}^{n,k} + r \operatorname{D} \tilde{\mathbf{u}}^{n,k} + \theta(\boldsymbol{\sigma}^n - \boldsymbol{\sigma}^{n,k})).$$

We will prove in the next section that the sequence $(\tilde{\mathbf{u}}^{n,k}, \boldsymbol{\sigma}^{n,k})_k$ defined by (11)–(12) converges to the solution $(\tilde{\mathbf{u}}^{n+1}, \boldsymbol{\sigma}^{n+1})$ of the system (9) (see Theorem 1). The pseudo-time relaxation $\theta(\boldsymbol{\sigma}^n - \boldsymbol{\sigma}^{n,k})$ added in (12) is essential as it improves the convergence of the fixed-point algorithm (11)–(12). Indeed, in Theorem 1 below, an estimate of the convergence rate, which depends on the parameter θ , of the sequence $(\tilde{\mathbf{u}}^{n,k}, \boldsymbol{\sigma}^{n,k})$ is derived. In the particular case $\theta = 0$, the numerical procedure (11)–(12) can be viewed as an Uzawa-like method applied to solve a viscoplastic problem, for which only convergence can be proved meaning that no estimate of the convergence rate is known.

3.2. Notations. The equations introduced before depend on parameters. Some parameters like $\Re e$ and $\Im i$ are physical ones, while others are numerical ones: r , θ , α and δt . All these parameters are always supposed to be positive.

For two vectors \mathbf{u} and \mathbf{v} in \mathbb{R}^d , we denote by $\mathbf{u} \cdot \mathbf{v}$ their inner product: $\mathbf{u} \cdot \mathbf{v} = \sum_{1 \leq i \leq d} u_i v_i$. For two tensors $\boldsymbol{\sigma}$ and $\boldsymbol{\tau}$ in $\mathbb{R}^{d \times d}$, we denote by $\boldsymbol{\sigma} : \boldsymbol{\tau}$ their inner product:

$$\boldsymbol{\sigma} : \boldsymbol{\tau} = \sum_{1 \leq i, j \leq d} \sigma_{ij} \tau_{ij}.$$

In both cases, the associated norm will be denoted $|\cdot|$.

For two real-valued functions f and g defined on the open set $\Omega \subset \mathbb{R}^d$, we will denote by $\langle f, g \rangle$ the $L^2(\Omega)$ -inner product, namely

$$\langle f, g \rangle = \int_{\Omega} f g.$$

The associated $L^2(\Omega)$ -norm will be denoted $\|\cdot\|_{L^2(\Omega)}$. For the sake of simplicity, the same notations for the inner product and the norm will be used throughout this paper for vectors in \mathbb{R}^d and tensors in $\mathbb{R}^{d \times d}$.

Also, other functional spaces may be considered in the sequel. In such cases, they are always indicated as subscripts: for instance $\|f\|_{H^{-1}(\Omega)}$ denotes the norm associated to the Sobolev space $H^{-1}(\Omega)$.

Let N be an integer and $\{t_n\}_{n \in \{0, \dots, N\}}$ be a sequence of discrete time levels in $[0, T]$. For simplicity, we consider a uniform discretisation, that is:

$$t_n = n \delta t \quad \text{with} \quad \delta t = \frac{T}{N}.$$

3.3. Well-posedness. At first we indicate that each problem previously introduced is well-posed.

✓ It is well known that the Stokes-Bingham system (8) has a solution $(\mathbf{u}, p, \boldsymbol{\sigma})$, see for instance [9] where the variational inequality formulation is used.

✓ The existence and uniqueness for the solution $(\tilde{\mathbf{u}}^{n+1}, \boldsymbol{\sigma}^{n+1})$ to system (9) result from the theory of variational inequalities too. The precise result for this system is proved in [7, p. 47].

✓ The system (10) is a classical correction step in projection methods: $\tilde{\mathbf{u}}^{n+1}$ and p^n given, it admits a unique solution $(\mathbf{u}^{n+1}, p^{n+1})$, up to an additive constant for the pressure field. Indeed, $\mathbf{u}^{n+1} = \mathbb{P}_H \tilde{\mathbf{u}}^{n+1}$ where \mathbb{P}_H is the orthogonal projector in $L^2(\Omega)^d$ onto the free-divergence vector space, and the pressure p^{n+1} is a solution of the following Poisson equation

$$\Delta p^{n+1} = \Delta p^n + \frac{1}{\alpha \delta t} \operatorname{div} \tilde{\mathbf{u}}^{n+1} \quad \text{supplemented with} \quad \left. \frac{\partial(p^{n+1} - p^n)}{\partial \mathbf{n}} \right|_{\partial \Omega} = 0.$$

✓ For each integer $n \in \mathbb{N}$, we show by induction on the integer k that each couple $(\tilde{\mathbf{u}}^{n,k}, \boldsymbol{\sigma}^{n,k})$ is well defined as the solution of the system (11)–(12). In particular the existence and uniqueness of $\tilde{\mathbf{u}}^{n,k}$ are ensured by the Lax-Milgram theorem.

3.4. Convergence results with respect to k .

Theorem 1. *We assume that*

$$2\theta + r \mathfrak{B}i \leq 2.$$

For each integer $n \in \mathbb{N}$, the sequence $(\tilde{\mathbf{u}}^{n,k}, \boldsymbol{\sigma}^{n,k})_k$ solutions of system (11)–(12) converges to $(\tilde{\mathbf{u}}^{n+1}, \boldsymbol{\sigma}^{n+1})$, solution of system (9), as k tends to $+\infty$.

Moreover the convergence is geometric with common ratio $1 - \theta$.

Proof. By denoting $\bar{\mathbf{u}}^k = \tilde{\mathbf{u}}^{n,k} - \tilde{\mathbf{u}}^{n+1}$ and $\bar{\boldsymbol{\sigma}}^k = \boldsymbol{\sigma}^{n,k} - \boldsymbol{\sigma}^{n+1}$ we obtain by subtracting (9) from (11)–(12) that, for all $k \geq 0$,

$$(13) \quad \begin{cases} \frac{1}{\delta t} \bar{\mathbf{u}}^k - \frac{1}{\mathfrak{R}e} \Delta \bar{\mathbf{u}}^k = \frac{\mathfrak{B}i}{\mathfrak{R}e} \operatorname{div} \bar{\boldsymbol{\sigma}}^k, \\ \bar{\mathbf{u}}^k \Big|_{\partial \Omega} = 0, \\ \bar{\boldsymbol{\sigma}}^{k+1} = \mathbb{P}(\boldsymbol{\sigma}^{n,k} + r \operatorname{D} \tilde{\mathbf{u}}^{n,k} + \theta(\boldsymbol{\sigma}^n - \boldsymbol{\sigma}^{n,k})) \\ \quad - \mathbb{P}(\boldsymbol{\sigma}^{n+1} + r \operatorname{D} \tilde{\mathbf{u}}^{n+1} + \theta(\boldsymbol{\sigma}^n - \boldsymbol{\sigma}^{n+1})). \end{cases}$$

We now take the inner product of the first equation in (13) by $\bar{\mathbf{u}}^k$ in $L^2(\Omega)$ to deduce

$$(14) \quad \frac{1}{\delta t} \|\bar{\mathbf{u}}^k\|_{L^2(\Omega)}^2 + \frac{1}{\mathfrak{R}e} \|\nabla \bar{\mathbf{u}}^k\|_{L^2(\Omega)}^2 = -\frac{\mathfrak{B}i}{\mathfrak{R}e} \langle \bar{\boldsymbol{\sigma}}^k, \operatorname{D} \bar{\mathbf{u}}^k \rangle.$$

Since \mathbb{P} is a projection operator, the last equation in (13) implies

$$|\bar{\boldsymbol{\sigma}}^{k+1}| \leq |(1 - \theta) \bar{\boldsymbol{\sigma}}^k + r \operatorname{D} \bar{\mathbf{u}}^k|.$$

Taking the $L^2(\Omega)$ -norm, we deduce (using $|\operatorname{D} \bar{\mathbf{u}}^k| \leq |\nabla \bar{\mathbf{u}}^k|$) that

$$(15) \quad \|\bar{\boldsymbol{\sigma}}^{k+1}\|_{L^2(\Omega)}^2 \leq (1 - \theta)^2 \|\bar{\boldsymbol{\sigma}}^k\|_{L^2(\Omega)}^2 + r^2 \|\nabla \bar{\mathbf{u}}^k\|_{L^2(\Omega)}^2 + 2r(1 - \theta) \langle \bar{\boldsymbol{\sigma}}^k, \operatorname{D} \bar{\mathbf{u}}^k \rangle.$$

Combining the equality (14) and the inequality (15) we obtain

$$(16) \quad \begin{aligned} & \frac{\mathfrak{B}i}{\mathfrak{R}e} \|\bar{\sigma}^{k+1}\|_{L^2(\Omega)}^2 + \frac{2r(1-\theta)}{\delta t} \|\bar{\mathbf{u}}^k\|_{L^2(\Omega)}^2 \\ & + \frac{r(2-2\theta-r\mathfrak{B}i)}{\mathfrak{R}e} \|\nabla \bar{\mathbf{u}}^k\|_{L^2(\Omega)}^2 \leq \frac{\mathfrak{B}i}{\mathfrak{R}e} (1-\theta)^2 \|\bar{\sigma}^k\|_{L^2(\Omega)}^2. \end{aligned}$$

We then deduce that, if $2\theta+r\mathfrak{B}i \leq 2$ all the coefficients in the left-hand side of the inequality (16) are non-negative. Therefore, we have

$$\begin{aligned} \|\bar{\sigma}^k\|_{L^2(\Omega)} & \leq (1-\theta)^k \|\bar{\sigma}^0\|_{L^2(\Omega)}, \\ \|\bar{\mathbf{u}}^k\|_{L^2(\Omega)} & \leq \sqrt{\frac{\mathfrak{B}i \delta t (1-\theta)}{2r \mathfrak{R}e}} (1-\theta)^k \|\bar{\sigma}^0\|_{L^2(\Omega)}, \end{aligned}$$

which concludes the proof of Theorem 1. \square

Note that, if $2\theta+r\mathfrak{B}i < 2$, we also have convergence in H^1 -norm for the velocity:

$$\|\nabla \bar{\mathbf{u}}^k\|_{L^2(\Omega)}^2 \leq \sqrt{\frac{\mathfrak{B}i}{r(2-2\theta-r\mathfrak{B}i)}} (1-\theta)^k \|\bar{\sigma}^0\|_{L^2(\Omega)}.$$

3.5. Stability result with respect to n .

Theorem 2 (Stability). *We assume that*

$$\alpha \geq 1, \quad r \mathfrak{B}i \leq 1 \quad \text{and} \quad \theta \leq 1/2.$$

The sequence $(\mathbf{u}^n, \tilde{\mathbf{u}}^n, p^n, \sigma^n)_n$ solutions of the system (9)–(10) is bounded.

We note that the assumptions of Theorem 2 implies that the assumption $2\theta+r\mathfrak{B}i \leq 2$ also holds for Theorem 1.

Proof. By definition of the sequence $(\sigma_n)_n$ and the projection \mathbb{P} , it is obvious that σ_n is bounded by unity. The method consists in deriving an estimate on the velocity sequences, and on the pressure sequence. We first take the inner product of the first equation of (9) with $2\delta t \tilde{\mathbf{u}}^{n+1}$ in $L^2(\Omega)^d$; using the identity

$$(17) \quad 2a(a-b) = a^2 - b^2 + (a-b)^2,$$

we derive

$$(18) \quad \begin{aligned} & \|\tilde{\mathbf{u}}^{n+1}\|_{L^2(\Omega)}^2 - \|\mathbf{u}^n\|_{L^2(\Omega)}^2 + \|\tilde{\mathbf{u}}^{n+1} - \mathbf{u}^n\|_{L^2(\Omega)}^2 + \frac{2\delta t}{\mathfrak{R}e} \|\nabla \tilde{\mathbf{u}}^{n+1}\|_{L^2(\Omega)}^2 \\ & = -2\delta t \langle \nabla p^n, \tilde{\mathbf{u}}^{n+1} \rangle - \frac{2\delta t \mathfrak{B}i}{\mathfrak{R}e} \langle \sigma^{n+1}, \mathbb{D} \tilde{\mathbf{u}}^{n+1} \rangle. \end{aligned}$$

The goal is to control the terms in the right-hand side (RHS) of the equality (18).

- *step 1 – control of $\langle \sigma^{n+1}, \mathbb{D} \tilde{\mathbf{u}}^{n+1} \rangle$*

Since \mathbb{P} is a projection operator, the stress tensor σ^{n+1} given by the second equation of the system (9) satisfies:

$$(19) \quad \begin{aligned} |\sigma^{n+1}|^2 & \leq |\sigma^{n+1} + r \mathbb{D} \tilde{\mathbf{u}}^{n+1} + \theta(\sigma^n - \sigma^{n+1})|^2 \\ & \leq |\sigma^{n+1}|^2 + r^2 |\mathbb{D} \tilde{\mathbf{u}}^{n+1}|^2 + \theta^2 |\sigma^n - \sigma^{n+1}|^2 + 2r \sigma^{n+1} : \mathbb{D} \tilde{\mathbf{u}}^{n+1} \\ & \quad + 2r\theta \mathbb{D} \tilde{\mathbf{u}}^{n+1} : (\sigma^n - \sigma^{n+1}) + 2\theta \sigma^{n+1} : (\sigma^n - \sigma^{n+1}). \end{aligned}$$

By invoking the Young inequality $2ab \leq a^2 + b^2$, we have

$$2r\theta D\tilde{\mathbf{u}}^{n+1} : (\boldsymbol{\sigma}^n - \boldsymbol{\sigma}^{n+1}) \leq r^2 |D\tilde{\mathbf{u}}^{n+1}|^2 + \theta^2 |\boldsymbol{\sigma}^n - \boldsymbol{\sigma}^{n+1}|^2,$$

and recalling the relation (17), we obtain

$$2\theta \boldsymbol{\sigma}^{n+1} : (\boldsymbol{\sigma}^n - \boldsymbol{\sigma}^{n+1}) = \theta |\boldsymbol{\sigma}^n|^2 - \theta |\boldsymbol{\sigma}^{n+1}|^2 - \theta |\boldsymbol{\sigma}^n - \boldsymbol{\sigma}^{n+1}|^2,$$

so that the inequality (19) rewrites

$$(20) \quad \begin{aligned} & \theta |\boldsymbol{\sigma}^{n+1}|^2 + (1 - 2\theta) \theta |\boldsymbol{\sigma}^{n+1} - \boldsymbol{\sigma}^n|^2 \\ & \leq 2r^2 |D\tilde{\mathbf{u}}^{n+1}|^2 + 2r \boldsymbol{\sigma}^{n+1} : D\tilde{\mathbf{u}}^{n+1} + \theta |\boldsymbol{\sigma}^n|^2. \end{aligned}$$

After performing an integration with respect to the space variable, we obtain

$$(21) \quad \begin{aligned} & \theta \|\boldsymbol{\sigma}^{n+1}\|_{L^2(\Omega)}^2 + (1 - 2\theta) \theta \|\boldsymbol{\sigma}^{n+1} - \boldsymbol{\sigma}^n\|_{L^2(\Omega)}^2 \\ & \leq 2r^2 \|\nabla \tilde{\mathbf{u}}^{n+1}\|_{L^2(\Omega)}^2 + 2r \langle \boldsymbol{\sigma}^{n+1}, D\tilde{\mathbf{u}}^{n+1} \rangle + \theta \|\boldsymbol{\sigma}^n\|_{L^2(\Omega)}^2. \end{aligned}$$

• *step 2 – control of $\langle \nabla p^n, \tilde{\mathbf{u}}^{n+1} \rangle$*

In order to estimate the pressure contribution in the RHS of (18), we proceed as follows. We take the inner product in $L^2(\Omega)^d$ of the first equation of (10) with the vector field $\frac{2(\alpha-1)\delta t}{\alpha} \mathbf{u}^{n+1}$ (which is divergence free) and use the identity (17) to derive

$$(22) \quad \frac{\alpha-1}{\alpha} (\|\mathbf{u}^{n+1}\|_{L^2(\Omega)}^2 - \|\tilde{\mathbf{u}}^{n+1}\|_{L^2(\Omega)}^2 + \|\mathbf{u}^{n+1} - \tilde{\mathbf{u}}^{n+1}\|_{L^2(\Omega)}^2) = 0.$$

We next take the inner product in $L^2(\Omega)^d$ of the same equation with $\frac{\delta t}{\alpha} (\mathbf{u}^{n+1} + \tilde{\mathbf{u}}^{n+1})$:

$$(23) \quad \frac{1}{\alpha} (\|\mathbf{u}^{n+1}\|_{L^2(\Omega)}^2 - \|\tilde{\mathbf{u}}^{n+1}\|_{L^2(\Omega)}^2) + \delta t \langle \nabla(p^{n+1} - p^n), \tilde{\mathbf{u}}^{n+1} \rangle = 0.$$

Finally, we take the inner product in $L^2(\Omega)^d$ of the first equation of (10) with the gradient term $\delta t^2 \nabla(p^{n+1} + p^n)$:

$$(24) \quad \alpha \delta t^2 (\|\nabla p^{n+1}\|_{L^2(\Omega)}^2 - \|\nabla p^n\|_{L^2(\Omega)}^2) - \delta t \langle \nabla(p^{n+1} + p^n), \tilde{\mathbf{u}}^{n+1} \rangle = 0.$$

Adding (22), (23) and (24), we obtain:

$$(25) \quad \begin{aligned} & \|\mathbf{u}^{n+1}\|_{L^2(\Omega)}^2 + \frac{\alpha-1}{\alpha} \|\mathbf{u}^{n+1} - \tilde{\mathbf{u}}^{n+1}\|_{L^2(\Omega)}^2 + \alpha \delta t^2 \|\nabla p^{n+1}\|_{L^2(\Omega)}^2 \\ & = 2\delta t \langle \nabla p^n, \tilde{\mathbf{u}}^{n+1} \rangle + \|\tilde{\mathbf{u}}^{n+1}\|_{L^2(\Omega)}^2 + \alpha \delta t^2 \|\nabla p^n\|_{L^2(\Omega)}^2. \end{aligned}$$

• *step 3 – final estimate and conclusion of the proof*

Combining the three results: (18) + $\frac{\delta t \mathfrak{B}i}{r \mathfrak{R}e}$ (21) + (25), we obtain

$$(26) \quad \begin{aligned} & \|\mathbf{u}^{n+1}\|_{L^2(\Omega)}^2 + \frac{\delta t \theta \mathfrak{B}i}{r \mathfrak{R}e} \|\boldsymbol{\sigma}^{n+1}\|_{L^2(\Omega)}^2 + \alpha \delta t^2 \|\nabla p^{n+1}\|_{L^2(\Omega)}^2 \\ & + \frac{2\delta t}{\mathfrak{R}e} (1 - r \mathfrak{B}i) \|\nabla \tilde{\mathbf{u}}^{n+1}\|_{L^2(\Omega)}^2 \\ & + \|\tilde{\mathbf{u}}^{n+1} - \mathbf{u}^n\|_{L^2(\Omega)}^2 + \frac{\alpha-1}{\alpha} \|\mathbf{u}^{n+1} - \tilde{\mathbf{u}}^{n+1}\|_{L^2(\Omega)}^2 \\ & + \frac{\delta t(1-2\theta)\theta \mathfrak{B}i}{r \mathfrak{R}e} \|\boldsymbol{\sigma}^{n+1} - \boldsymbol{\sigma}^n\|_{L^2(\Omega)}^2 \\ & \leq \|\mathbf{u}^n\|_{L^2(\Omega)}^2 + \frac{\delta t \theta \mathfrak{B}i}{r \mathfrak{R}e} \|\boldsymbol{\sigma}^n\|_{L^2(\Omega)}^2 + \alpha \delta t^2 \|\nabla p^n\|_{L^2(\Omega)}^2. \end{aligned}$$

If we denote by $y_n = \|\mathbf{u}^n\|_{L^2(\Omega)}^2 + \frac{\delta t \theta \mathfrak{B}i}{r \mathfrak{R}e} \|\boldsymbol{\sigma}^n\|_{L^2(\Omega)}^2 + \alpha \delta t^2 \|\nabla p^n\|_{L^2(\Omega)}^2$ then the previous estimate indicates in particular that $y_{n+1} \leq y_n$ as soon as the following conditions

$$\alpha \geq 1, \quad 1 - r \mathfrak{B}i \geq 0 \quad \text{and} \quad 1 - 2\theta \geq 0$$

hold. The sequence $(y_n)_n$ is then bounded, which implies a bound on the sequences $(\mathbf{u}^n)_n$, $(p^n)_n$ and $(\boldsymbol{\sigma}^n)_n$. Recalling (26), a bound follows on $(\tilde{\mathbf{u}}^{n+1} - \mathbf{u}^n)_n$. As a consequence, with the help of (23), the sequence $(\tilde{\mathbf{u}}^n)_n$ is also bounded. This completes the proof of Theorem 2. \square

3.6. Convergence results with respect to n .

Theorem 3 (Velocity convergence). *We assume that*

$$\alpha \geq 1, \quad 3r \mathfrak{B}i \leq 1, \quad \theta \leq 1/3 \quad \text{and} \quad \delta t \leq 1/2.$$

If there exists a regular solution $(\mathbf{u}, p, \boldsymbol{\sigma})$ of (8) then the sequence $(\mathbf{u}^n)_n$ issued from the system (9)–(10) converges to \mathbf{u} as n tends to $+\infty$. More precisely, there exists a constant C depending on $\mathfrak{R}e$, $\mathfrak{B}i$, r , α and T (but neither on θ nor on δt), such that for all $0 \leq n \leq N$, we have

$$\|\mathbf{u}(t_n) - \mathbf{u}^n\|_{L^2(\Omega)}^2 + \delta t \sum_{k=0}^n \|\mathbf{u}(t_k) - \mathbf{u}^k\|_{H^1(\Omega)}^2 \leq C(\theta \delta t + \delta t^2).$$

Remark 3.

- (1) *We say that a solution $(\mathbf{u}, p, \boldsymbol{\sigma})$ of (8) is regular if we have*

$$\begin{aligned} \partial_t^2 \mathbf{u} &\in L^2(0, T; H^{-1}(\Omega)^d), \\ \partial_t \nabla p &\in L^2(0, T; L^2(\Omega)^d), \\ \partial_t \boldsymbol{\sigma} &\in L^2(0, T; L^2(\Omega)^{d \times d}). \end{aligned}$$

The above assumptions for velocity and pressure are classically made when conducting the error analysis of the projection schemes applied to the temporal discretisation of the Navier-Stokes equations (see for instance [23, 24]).

- (2) *The error estimate derived in Theorem 3 possesses two contributions. The first one, bounded by $\theta \delta t$, corresponds to the error due to the “approximation” of the Bingham projection, while the second one, of the order of δt^2 , is the usual error estimate obtained when time projection scheme are applied to the Navier-Stokes equations (see [23, 24]).*
- (3) *The hypotheses $3r \mathfrak{B}i \leq 1$ and $\theta \leq 1/3$ are not optimal. We will see during the sketch of the proof that these constraints on the parameters are due to use of the Young inequality $2ab \leq a^2 + b^2$. This can be improved if finer estimates are used, namely $2ab \leq \varepsilon a^2 + b^2/\varepsilon$ for any $\varepsilon > 0$. Nevertheless, the price to pay will be a larger numerical value of the constant C .*

Proof. Let $(\mathbf{u}, p, \boldsymbol{\sigma})$ be a regular solution of system (8) and let $(\mathbf{u}^n, \tilde{\mathbf{u}}^n, p^n, \boldsymbol{\sigma}^n)_n$ be the solution of the discrete system (9)–(10). We introduce the following quantities

$$\begin{aligned} \mathbf{e}^n &= \mathbf{u}(t_n) - \mathbf{u}^n, & \tilde{\mathbf{e}}^n &= \mathbf{u}(t_n) - \tilde{\mathbf{u}}^n, \\ q^n &= p(t_n) - p^n, & \mathbf{s}^n &= \boldsymbol{\sigma}(t_n) - \boldsymbol{\sigma}^n. \end{aligned}$$

Subtracting the system (9)–(10) from the system (8) taken at time t_{n+1} leads to

$$(27) \quad \begin{cases} \frac{\tilde{\mathbf{e}}^{n+1} - \mathbf{e}^n}{\delta t} + \nabla(p(t_{n+1}) - p^n) - \frac{1}{\mathfrak{R}_e} \Delta \tilde{\mathbf{e}}^{n+1} = \frac{\mathfrak{B}i}{\mathfrak{R}_e} \operatorname{div} \mathbf{s}^{n+1} + \mathbf{R}^n, \\ \frac{\mathbf{e}^{n+1} - \tilde{\mathbf{e}}^{n+1}}{\delta t} - \alpha \nabla(p^{n+1} - p^n) = 0, \\ \operatorname{div} \mathbf{e}^{n+1} = 0, \\ \mathbf{s}^{n+1} = \mathbb{P}(\boldsymbol{\sigma}(t_{n+1}) + r \mathbf{D}\mathbf{u}(t_{n+1})) \\ \quad - \mathbb{P}(\boldsymbol{\sigma}^{n+1} + r \mathbf{D}\tilde{\mathbf{u}}^{n+1} + \theta(\mathbf{s}^{n+1} - \mathbf{s}^n) - \theta \Sigma^n), \\ \tilde{\mathbf{e}}^{n+1} \Big|_{\partial\Omega} = \mathbf{0}, \quad \mathbf{e}^{n+1} \cdot \mathbf{n} \Big|_{\partial\Omega} = 0, \end{cases}$$

where the truncation error terms \mathbf{R}^n and Σ^n are given by:

$$(28) \quad \begin{aligned} \mathbf{R}^n &= \frac{\mathbf{u}(t_{n+1}) - \mathbf{u}(t_n)}{\delta t} - \partial_t \mathbf{u}(t_{n+1}) = \frac{1}{\delta t} \int_{t_n}^{t_{n+1}} (t_n - t) \partial_t^2 \mathbf{u}(t) dt, \\ \Sigma^n &= \sigma(t_{n+1}) - \sigma(t_n) = \int_{t_n}^{t_{n+1}} \partial_t \sigma(t) dt. \end{aligned}$$

Taking the inner product in $L^2(\Omega)^d$ between the first equation of (27) and $2\delta t \tilde{\mathbf{e}}^{n+1}$ and recalling (17), we deduce

$$(29) \quad \begin{aligned} &\|\tilde{\mathbf{e}}^{n+1}\|_{L^2(\Omega)}^2 - \|\mathbf{e}^n\|_{L^2(\Omega)}^2 + \|\tilde{\mathbf{e}}^{n+1} - \mathbf{e}^n\|_{L^2(\Omega)}^2 + \frac{2\delta t}{\mathfrak{R}_e} \|\nabla \tilde{\mathbf{e}}^{n+1}\|_{L^2(\Omega)}^2 \\ &+ 2\delta t \langle \nabla(p(t_{n+1}) - p^n), \tilde{\mathbf{e}}^{n+1} \rangle = -\frac{2\delta t \mathfrak{B}i}{\mathfrak{R}_e} \langle \mathbf{s}^{n+1}, \mathbf{D}\tilde{\mathbf{e}}^{n+1} \rangle + 2\delta t \langle \mathbf{R}^n, \tilde{\mathbf{e}}^{n+1} \rangle. \end{aligned}$$

We now take the inner product in $L^2(\Omega)^d$ of the second equation of (27) with $\frac{2(\alpha-1)\delta t}{\alpha} \mathbf{e}^{n+1}$, and with $\frac{\delta t}{\alpha} (\mathbf{e}^{n+1} + \tilde{\mathbf{e}}^{n+1})$. We add the resulting relations and deduce

$$(30) \quad \begin{aligned} &\|\mathbf{e}^{n+1}\|_{L^2(\Omega)}^2 - \|\tilde{\mathbf{e}}^{n+1}\|_{L^2(\Omega)}^2 + \frac{\alpha-1}{\alpha} \|\mathbf{e}^{n+1} - \tilde{\mathbf{e}}^{n+1}\|_{L^2(\Omega)}^2 \\ &- \delta t \langle \nabla(p^{n+1} - p^n), \tilde{\mathbf{e}}^{n+1} \rangle = 0. \end{aligned}$$

Adding equations (29) and (30), we arrive at

$$(31) \quad \begin{aligned} &\|\mathbf{e}^{n+1}\|_{L^2(\Omega)}^2 - \|\mathbf{e}^n\|_{L^2(\Omega)}^2 + \|\tilde{\mathbf{e}}^{n+1} - \mathbf{e}^n\|_{L^2(\Omega)}^2 + \frac{\alpha-1}{\alpha} \|\mathbf{e}^{n+1} - \tilde{\mathbf{e}}^{n+1}\|_{L^2(\Omega)}^2 \\ &+ \frac{2\delta t}{\mathfrak{R}_e} \|\nabla \tilde{\mathbf{e}}^{n+1}\|_{L^2(\Omega)}^2 + \delta t \langle \nabla(2p(t_{n+1}) - (p^{n+1} + p^n)), \tilde{\mathbf{e}}^{n+1} \rangle \\ &= -\frac{2\delta t \mathfrak{B}i}{\mathfrak{R}_e} \langle \mathbf{s}^{n+1}, \mathbf{D}\tilde{\mathbf{e}}^{n+1} \rangle + 2\delta t \langle \mathbf{R}^n, \tilde{\mathbf{e}}^{n+1} \rangle. \end{aligned}$$

By introducing

$$(32) \quad \mathbf{Q}^n = p(t_{n+1}) - p(t_n),$$

we have

$$\begin{aligned} p^{n+1} - p^n &= \mathbf{Q}^n - (q^{n+1} - q^n), \\ 2p(t_{n+1}) - (p^{n+1} + p^n) &= \mathbf{Q}^n + (q^{n+1} + q^n). \end{aligned}$$

Taking the inner product of the second equation of (27) with the pressure gradient term $\delta t^2 \nabla(2p(t_{n+1}) - (p^{n+1} - p^n))$ and using the above relations, we derive

$$\begin{aligned} \delta t \langle \nabla(2p(t_{n+1}) - (p^{n+1} - p^n)), \tilde{\mathbf{e}}^{n+1} \rangle &= \alpha \delta t^2 (\|\nabla q^{n+1}\|_{L^2(\Omega)}^2 - \|\nabla q^n\|_{L^2(\Omega)}^2) \\ &\quad - \alpha \delta t^2 \|\nabla Q^n\|_{L^2(\Omega)}^2 - 2\alpha \delta t^2 \langle \nabla Q^n, \nabla q^n \rangle. \end{aligned}$$

Now, by reporting this equality in (31), we obtain

$$\begin{aligned} (33) \quad &\|\mathbf{e}^{n+1}\|_{L^2(\Omega)}^2 - \|\mathbf{e}^n\|_{L^2(\Omega)}^2 + \|\tilde{\mathbf{e}}^{n+1} - \mathbf{e}^n\|_{L^2(\Omega)}^2 + \frac{\alpha - 1}{\alpha} \|\mathbf{e}^{n+1} - \tilde{\mathbf{e}}^{n+1}\|_{L^2(\Omega)}^2 \\ &+ \frac{2\delta t}{\mathfrak{R}e} \|\nabla \tilde{\mathbf{e}}^{n+1}\|_{L^2(\Omega)}^2 + \alpha \delta t^2 (\|\nabla q^{n+1}\|_{L^2(\Omega)}^2 - \|\nabla q^n\|_{L^2(\Omega)}^2) \\ &= -\frac{2\delta t \mathfrak{B}i}{\mathfrak{R}e} \langle \mathbf{s}^{n+1}, \mathbf{D}\tilde{\mathbf{e}}^{n+1} \rangle + 2\delta t \langle \mathbf{R}^n, \tilde{\mathbf{e}}^{n+1} \rangle + \alpha \delta t^2 \|\nabla Q^n\|_{L^2(\Omega)}^2 \\ &\quad + 2\alpha \delta t^2 \langle \nabla Q^n, \nabla q^n \rangle. \end{aligned}$$

• *step 1 – control of $\langle \mathbf{s}^{n+1}, \mathbf{D}\tilde{\mathbf{e}}^{n+1} \rangle$*

The term $\langle \mathbf{s}^{n+1}, \mathbf{D}\tilde{\mathbf{e}}^{n+1} \rangle$ in the RHS of (33) is due to the plastic stress tensor and is a new contribution compared to the classical estimates for the projection scheme for the Stokes equations. This term is bounded as it follows. Since \mathbb{P} is a projection, we have

$$|\mathbf{s}^{n+1}| \leq |\mathbf{s}^{n+1} + r \mathbf{D}\tilde{\mathbf{e}}^{n+1} + \theta(\mathbf{s}^n - \mathbf{s}^{n+1}) + \theta \Sigma^n|.$$

By taking the square of this inequality and by expanding the resulting right-hand side, we deduce

$$\begin{aligned} (34) \quad &|\mathbf{s}^{n+1}|^2 \leq |\mathbf{s}^{n+1}|^2 + r^2 |\mathbf{D}\tilde{\mathbf{e}}^{n+1}|^2 \\ &\quad + \theta^2 |\mathbf{s}^n - \mathbf{s}^{n+1}|^2 + \theta^2 |\Sigma^n|^2 \\ &\quad + \underbrace{2r \mathbf{s}^{n+1} : \mathbf{D}\tilde{\mathbf{e}}^{n+1}}_{=a_1} + \underbrace{2\theta \mathbf{s}^{n+1} : (\mathbf{s}^n - \mathbf{s}^{n+1})}_{=a_2} \\ &\quad + \underbrace{2\theta \mathbf{s}^{n+1} : \Sigma^n}_{=a_3} + \underbrace{2r\theta \mathbf{D}\tilde{\mathbf{e}}^{n+1} : (\mathbf{s}^n - \mathbf{s}^{n+1})}_{=a_4} \\ &\quad + \underbrace{2r\theta \mathbf{D}\tilde{\mathbf{e}}^{n+1} : \Sigma^n}_{=a_5} + \underbrace{2\theta^2 (\mathbf{s}^n - \mathbf{s}^{n+1}) : \Sigma^n}_{=a_6}. \end{aligned}$$

Note that the integral of the term a_1 with respect to the space variable $\mathbf{x} \in \Omega$ is exactly the term we aim to control. We therefore keep it unchanged. Using the identity (17), we rewrite the term a_2 as

$$a_2 = -\theta |\mathbf{s}^{n+1}|^2 + \theta |\mathbf{s}^n|^2 - \theta |\mathbf{s}^{n+1} - \mathbf{s}^n|^2.$$

With the help of the Young inequality, the term a_3 is bounded from above as it follows

$$a_3 \leq \theta \delta t |\mathbf{s}^{n+1}|^2 + \frac{\theta}{\delta t} |\Sigma^n|^2.$$

By bounding similarly the other terms in the right-hand side of (34), namely a_4 , a_5 and a_6 , we deduce the estimate

$$\begin{aligned} &\theta(1 - \delta t) |\mathbf{s}^{n+1}|^2 + \theta(1 - 3\theta) |\mathbf{s}^{n+1} - \mathbf{s}^n|^2 \leq 2r \mathbf{s}^{n+1} : \mathbf{D}\tilde{\mathbf{e}}^{n+1} \\ &\quad + \theta |\mathbf{s}^n|^2 + 3r^2 |\mathbf{D}\tilde{\mathbf{e}}^{n+1}|^2 + \theta \left(\frac{1}{\delta t} + 3\theta \right) |\Sigma^n|^2. \end{aligned}$$

Integrating the above inequality with respect to the spatial variable $\mathbf{x} \in \Omega$ leads to

$$(35) \quad \begin{aligned} & \theta \left[(1 - \delta t) \|\mathbf{s}^{n+1}\|_{L^2(\Omega)}^2 - \|\mathbf{s}^n\|_{L^2(\Omega)}^2 \right] + \theta(1 - 3\theta) \|\mathbf{s}^{n+1} - \mathbf{s}^n\|_{L^2(\Omega)}^2 \\ & \leq 2r \langle \mathbf{s}^{n+1}, D\tilde{\mathbf{e}}^{n+1} \rangle + 3r^2 \|D\tilde{\mathbf{e}}^{n+1}\|_{L^2(\Omega)}^2 + \theta \left(\frac{1}{\delta t} + 3\theta \right) \|\Sigma^n\|_{L^2(\Omega)}^2. \end{aligned}$$

• *step 2 – final estimate*

By adding the two results (33) and $\frac{\delta t \mathfrak{B}i}{r \mathfrak{R}e}$ (35) and recalling that $|D\tilde{\mathbf{e}}^{n+1}| \leq |\nabla \tilde{\mathbf{e}}^{n+1}|$, we obtain

$$(36) \quad \begin{aligned} & \|\mathbf{e}^{n+1}\|_{L^2(\Omega)}^2 - \|\mathbf{e}^n\|_{L^2(\Omega)}^2 + \frac{\alpha - 1}{\alpha} \|\mathbf{e}^{n+1} - \tilde{\mathbf{e}}^{n+1}\|_{L^2(\Omega)}^2 \\ & + \|\tilde{\mathbf{e}}^{n+1} - \mathbf{e}^n\|_{L^2(\Omega)}^2 + \frac{\delta t}{\mathfrak{R}e} (2 - 3r \mathfrak{B}i) \|\nabla \tilde{\mathbf{e}}^{n+1}\|_{L^2(\Omega)}^2 \\ & + \frac{\theta \delta t \mathfrak{B}i}{r \mathfrak{R}e} \left[(1 - \delta t) \|\mathbf{s}^{n+1}\|_{L^2(\Omega)}^2 - \|\mathbf{s}^n\|_{L^2(\Omega)}^2 \right] \\ & + \frac{\theta(1 - 3\theta) \delta t \mathfrak{B}i}{r \mathfrak{R}e} \|\mathbf{s}^{n+1} - \mathbf{s}^n\|_{L^2(\Omega)}^2 \\ & + \alpha \delta t^2 \left[\|\nabla q^{n+1}\|_{L^2(\Omega)}^2 - \|\nabla q^n\|_{L^2(\Omega)}^2 \right] \\ & \leq \underbrace{2\delta t \langle \mathbf{R}^n, \tilde{\mathbf{e}}^{n+1} \rangle}_{b_1} + \theta(1 + 3\theta \delta t) \frac{\mathfrak{B}i}{r \mathfrak{R}e} \|\Sigma^n\|_{L^2(\Omega)}^2 \\ & \quad + \alpha \delta t^2 \|\nabla Q^n\|_{L^2(\Omega)}^2 + \underbrace{2\alpha \delta t^2 \langle \nabla Q^n, \nabla q^n \rangle}_{b_2}. \end{aligned}$$

The term b_1 is treated by invoking the duality between H^{-1} and H_0^1 , and the Young inequality, so that

$$\begin{aligned} b_1 & \leq 2\delta t \|\mathbf{R}^n\|_{H^{-1}(\Omega)} \|\tilde{\mathbf{e}}^{n+1}\|_{H_0^1(\Omega)} \\ & \leq \frac{\delta t}{\mathfrak{R}e} \|\nabla \tilde{\mathbf{e}}^{n+1}\|_{L^2(\Omega)}^2 + \delta t \mathfrak{R}e \|\mathbf{R}^n\|_{H^{-1}(\Omega)}^2. \end{aligned}$$

With the help of the Young inequality, an upper bound for the term b_2 is obtained as it follows

$$\begin{aligned} b_2 & \leq 2\alpha \delta t^2 \|\nabla Q^n\|_{L^2(\Omega)} \|\nabla q^n\|_{L^2(\Omega)} \\ & \leq \alpha \delta t \|\nabla Q^n\|_{L^2(\Omega)}^2 + \alpha \delta t^3 \|\nabla q^n\|_{L^2(\Omega)}^2. \end{aligned}$$

Reporting these bounds on b_1 and b_2 in (36), we obtain

$$\begin{aligned}
(37) \quad & \|e^{n+1}\|_{L^2(\Omega)}^2 - \|e^n\|_{L^2(\Omega)}^2 + \frac{\alpha-1}{\alpha} \|e^{n+1} - \tilde{e}^{n+1}\|_{L^2(\Omega)}^2 \\
& + \|\tilde{e}^{n+1} - e^n\|_{L^2(\Omega)}^2 + \frac{\delta t}{\mathfrak{R}e} (1 - 3r \mathfrak{B}i) \|\nabla \tilde{e}^{n+1}\|_{L^2(\Omega)}^2 \\
& + \frac{\theta \delta t \mathfrak{B}i}{r \mathfrak{R}e} \left[(1 - \delta t) \|s^{n+1}\|_{L^2(\Omega)}^2 - \|s^n\|_{L^2(\Omega)}^2 \right] \\
& + \frac{\theta(1-3\theta) \delta t \mathfrak{B}i}{r \mathfrak{R}e} \|s^{n+1} - s^n\|_{L^2(\Omega)}^2 \\
& + \alpha \delta t^2 \left[\|\nabla q^{n+1}\|_{L^2(\Omega)}^2 - \|\nabla q^n\|_{L^2(\Omega)}^2 \right] \\
& \leq \delta t \mathfrak{R}e \|R^n\|_{H^{-1}(\Omega)}^2 + \theta(1+3\theta \delta t) \frac{\mathfrak{B}i}{r \mathfrak{R}e} \|\Sigma^n\|_{L^2(\Omega)}^2 \\
& \quad + \alpha \delta t (1 + \delta t) \|\nabla Q^n\|_{L^2(\Omega)}^2 + \alpha \delta t^3 \|\nabla q^n\|_{L^2(\Omega)}^2.
\end{aligned}$$

• *step 3 – the Gronwall lemma*

If the following conditions

$$\alpha \geq 1, \quad 3r \mathfrak{B}i \leq 1, \quad \theta \leq 1/3,$$

hold, we deduce from the above inequality

$$(38) \quad y_{n+1} + z_{n+1} \leq \frac{(1 + \delta t)}{(1 - \delta t)} y_n + \varepsilon_n,$$

where

$$\begin{aligned}
y_n &= (1 - \delta t) \left(\|e^n\|_{L^2(\Omega)}^2 + \frac{\mathfrak{B}i}{r \mathfrak{R}e} \theta \delta t \|s^n\|_{L^2(\Omega)}^2 + \alpha \delta t^2 \|\nabla q^n\|_{L^2(\Omega)}^2 \right), \\
z_n &= \frac{(1 - 3r \mathfrak{B}i)}{\mathfrak{R}e} \delta t \|\nabla \tilde{e}^{n+1}\|_{L^2(\Omega)}^2,
\end{aligned}$$

and

$$\varepsilon_n = \delta t \mathfrak{R}e \|R^n\|_{H^{-1}(\Omega)}^2 + \theta(1+3\theta \delta t) \frac{\mathfrak{B}i}{r \mathfrak{R}e} \|\Sigma^n\|_{L^2(\Omega)}^2 + \alpha \delta t (1 + \delta t) \|\nabla Q^n\|_{L^2(\Omega)}^2.$$

By applying the discrete Gronwall lemma to (38), we derive, for any $1 \leq m \leq N$,

$$y_m + \sum_{n=1}^m z_n \leq \left(\frac{1 + \delta t}{1 - \delta t} \right)^m \left(y_0 + \sum_{n=0}^{m-1} \varepsilon_n \right).$$

Noting that, for $\delta t \leq \frac{1}{2}$, we have $\frac{1+\delta t}{1-\delta t} \leq (1 + \delta t)^3 \leq \exp(3\delta t)$, then for all $1 \leq m \leq N$, the following inequality holds

$$(39) \quad y_m + \sum_{n=1}^m z_n \leq \exp(3T) \left(y_0 + \sum_{n=0}^{m-1} \varepsilon_n \right).$$

Recalling that, by definition, $e^0 = 0$ the proof of the theorem relies on deriving a proper bound for the term $\sum_{j=0}^{n-1} \varepsilon_j$ in the above inequality.

• *step 4 – control of the error ε_n*

We now derive estimates of the term ε_n with respect to the parameters θ and δt . From the definition of Σ^n (in (28)), we have

$$\|\Sigma^n\|_{L^2(\Omega)}^2 = \left\| \int_{t_n}^{t_{n+1}} \partial_t \sigma(t) dt \right\|_{L^2(\Omega)}^2 \leq \delta t \int_{t_n}^{t_{n+1}} \|\partial_t \sigma(t)\|_{L^2(\Omega)}^2 dt.$$

Similarly for Q^n (in (32)), we obtain

$$\|\nabla Q^n\|_{L^2(\Omega)}^2 \leq \delta t \int_{t_n}^{t_{n+1}} \|\partial_t \nabla p\|_{L^2(\Omega)}^2 dt,$$

and finally for R^n (in (28)), we have

$$\begin{aligned} \|R^n\|_{H^{-1}(\Omega)}^2 &= \frac{1}{\delta t^2} \left\| \int_{t_n}^{t_{n+1}} (t_n - t) \partial_t^2 \mathbf{u}(t) dt \right\|_{H^{-1}(\Omega)}^2 \\ &\leq \frac{1}{\delta t^2} \left(\int_{t_n}^{t_{n+1}} (t - t_n)^2 dt \right) \left(\int_{t_n}^{t_{n+1}} \|\partial_t^2 \mathbf{u}(t)\|_{H^{-1}(\Omega)}^2 dt \right) \\ &\leq \frac{\delta t}{3} \int_{t_n}^{t_{n+1}} \|\partial_t^2 \mathbf{u}(t)\|_{H^{-1}(\Omega)}^2 dt. \end{aligned}$$

Reporting these estimates in the above definition of ε_n , assuming the regularity of the solution (\mathbf{u}, p, σ) and summing up from $n = 0$ to $m - 1$, leads to

$$(40) \quad \begin{aligned} \sum_{n=0}^{m-1} \varepsilon_n &\leq \delta t^2 \left(\frac{\Re e}{3} \|\partial_t^2 \mathbf{u}\|_{L^2(0,T;H^{-1}(\Omega)^d)}^2 + \alpha (1 + \delta t) \|\partial_t \nabla p\|_{L^2(0,T;L^2(\Omega)^d)}^2 \right) \\ &\quad + \theta \delta t (1 + 3\theta \delta t) \frac{\Im i}{r \Re e} \|\partial_t \sigma\|_{L^2(0,T;L^2(\Omega)^{d \times d})}^2. \end{aligned}$$

• *step 6 – conclusion of the proof*

Thanks to (40), the inequality (39) now reads, for all $1 \leq m \leq N$,

$$y_m + \sum_{n=1}^m z_n \leq \exp(3T) \left(c_1 \theta \delta t + c_2 \delta t^2 \right)$$

with

$$\begin{cases} c_1 = \frac{\Im i}{r \Re e} \left(\|\mathbf{s}^0\|_{L^2(\Omega)}^2 + \frac{3}{2} \|\partial_t \sigma\|_{L^2(0,T;L^2(\Omega)^{d \times d})}^2 \right), \\ c_2 = \frac{\Re e}{3} \|\partial_t^2 \mathbf{u}\|_{L^2(0,T;H^{-1}(\Omega)^d)}^2 + \frac{3\alpha}{2} \|\partial_t \nabla p\|_{L^2(0,T;L^2(\Omega)^d)}^2 + \alpha \|\nabla q^0\|_{L^2(\Omega)}^2. \end{cases}$$

Recalling the definition of y_n and z_n , and that $1 - \delta t \geq \frac{1}{2}$, we deduce that

$$\|\mathbf{e}^n\|_{L^2(\Omega)}^2 \leq 2 \exp(3T) \left(c_1 \theta \delta t + c_2 \delta t^2 \right),$$

and

$$\delta t \sum_{j=1}^n \|\nabla \tilde{\mathbf{e}}^j\|_{L^2(\Omega)}^2 \leq \frac{\Re e}{(1 - 3r \Im i)} \exp(3T) \left(c_1 \theta \delta t + c_2 \delta t^2 \right).$$

Thanks to the inequality (see [26, Remark 1.6])

$$\|\mathbf{e}^n\|_{H^1(\Omega)} \leq C(\Omega) \|\tilde{\mathbf{e}}^n\|_{H^1(\Omega)}$$

we conclude the proof of Theorem 3. \square

3.7. Some remarks.

✓ Convergence of the velocity

Theorem 3 can be interpreted in several ways. The first one shows that, selecting θ of order δt , the discrete velocity field is a first-order approximation of the solution \mathbf{u} of the Stokes-Bingham equation (8). The second one proves that, for a fixed value of the parameter θ (satisfying the assumption $\theta \leq 1/3$), the scheme converges to the solution of the Stokes-Bingham problem (8). This important property shows that our bi-projection scheme (9)–(10)–(11)–(12) is very different than the common regularisation method, studied for instance in [28], which rewrites the plastic tensor as

$$\boldsymbol{\sigma}_\varepsilon = \frac{\mathbf{D}\mathbf{u}}{\sqrt{|\mathbf{D}\mathbf{u}|^2 + \varepsilon^2}} \quad \text{instead of} \quad \boldsymbol{\sigma} = \frac{\mathbf{D}\mathbf{u}}{|\mathbf{D}\mathbf{u}|}.$$

Indeed, the error derived for the regularised problem is cumulative, that is bounded by $\delta t + \sqrt{\varepsilon}$ (see Theorem 4.7 [28]), while the error obtained in Theorem 3 is bounded by $\delta t + \sqrt{\delta t \theta}$. The discrete velocity field solution of our projection scheme converges to the solution of the Stokes-Bingham equations whatever the value of $\theta \leq 1/3$ is. In the following section, we will also see that the projection scheme proposed in the present article captures the flow cessation property in finite time characterising viscoplastic Bingham flows.

✓ Convergence of the stress tensor

Theorem 3 does not provide a convergence result for the stress tensor sequence. Nevertheless, the sequence $(\boldsymbol{\sigma}^n)_n$ is well defined and bounded so that we have a convergence up to a subsequence. However, for a fixed value of $\theta > 0$, we can prove that there exists a constant $C_\theta > 0$ such that we have the following result:

The sequence $(\boldsymbol{\sigma}^n)_n$ satisfies

$$(41) \quad \|\bar{\boldsymbol{\sigma}}(t_n) - \boldsymbol{\sigma}^n\|_{L^2(\Omega)}^2 \leq C_\theta \delta t,$$

where $(\bar{\mathbf{u}}, \bar{p}, \bar{\boldsymbol{\sigma}})$ is the solution of

$$(42) \quad \begin{cases} \partial_t \bar{\mathbf{u}} + \bar{\mathbf{u}} \cdot \nabla \bar{\mathbf{u}} + \nabla \bar{p} - \frac{1}{\mathfrak{R}e} \Delta \bar{\mathbf{u}} = \frac{\mathfrak{B}i}{\mathfrak{R}e} \operatorname{div} \bar{\boldsymbol{\sigma}}, \\ \operatorname{div} \bar{\mathbf{u}} = 0, \\ \bar{\boldsymbol{\sigma}} = \mathbb{P}(\bar{\boldsymbol{\sigma}} + r \mathbf{D}\bar{\mathbf{u}} - \delta t \theta \partial_t \bar{\boldsymbol{\sigma}}). \end{cases}$$

Indeed the proof is very similar to the one of Theorem 3. The only change is in the value of the residual tensor which becomes

$$\bar{\Sigma}^n = \bar{\boldsymbol{\sigma}}(t_{n+1}) - \bar{\boldsymbol{\sigma}}(t_n) - \delta t \partial_t \bar{\boldsymbol{\sigma}}(t_{n+1}) = \int_{t_n}^{t_{n+1}} (t_n - t) \partial_t^2 \bar{\boldsymbol{\sigma}}(t) dt.$$

Under some regularity assumptions on $\bar{\boldsymbol{\sigma}}$, we deduce that

$$\begin{aligned} \sum_{n=0}^N \|\bar{\Sigma}^n\|_{L^2(\Omega)}^2 &= \sum_{n=0}^N \left\| \int_{t_n}^{t_{n+1}} (t_n - t) \partial_t^2 \bar{\boldsymbol{\sigma}}(t) dt \right\|_{L^2(\Omega)}^2 \\ &\leq \sum_{n=0}^N \left(\int_{t_n}^{t_{n+1}} (t - t_n) dt \right) \left(\int_{t_n}^{t_{n+1}} (t - t_n) \|\partial_t^2 \bar{\boldsymbol{\sigma}}(t)\|_{L^2(\Omega)}^2 dt \right) \\ &\leq \frac{\delta t^2}{2} \int_0^T t \|\partial_t^2 \bar{\boldsymbol{\sigma}}(t)\|_{L^2(\Omega)}^2 dt = \mathcal{O}(\delta t^2). \end{aligned}$$

In this case, the cumulative error $\sum_{n=0}^{N-1} \varepsilon_n$ satisfies

$$\sum_{n=0}^{N-1} \varepsilon_n \leq C \delta t^2,$$

where C is an appropriate constant depending on the data and on the solution (\mathbf{u}, p) of the Stokes-Bingham problem. This result implies the result (41).

Note also that with this error estimate on the stress tensor, we may expect to obtain an estimate of convergence on the pressure like (see theorem 2 on page 72 in [23] and [24] for the proof):

$$(43) \quad \delta t \sum_{k=0}^n \|\bar{p}(t_k) - p^n\|_{L^2(\Omega)}^2 \leq C_\theta \delta t^2.$$

4. NUMERICAL RESULTS

In this section we present numerical simulations of solutions of the following equations modelling the motion of an incompressible Bingham viscoplastic medium:

$$(44) \quad \begin{cases} \partial_t \mathbf{u} - \frac{1}{\mathfrak{R}e} \Delta \mathbf{u} + \operatorname{div}(\mathbf{u} \otimes \mathbf{u}) + \nabla p = \frac{\mathfrak{B}i}{\mathfrak{R}e} \operatorname{div} \boldsymbol{\sigma}, \\ \operatorname{div} \mathbf{u} = 0, \\ \boldsymbol{\sigma} = \mathbb{P}(\boldsymbol{\sigma} + r \operatorname{D}\mathbf{u}), \\ \mathbf{u}|_{\partial\Omega} = \mathbf{u}_b, \end{cases}$$

where \mathbf{u}_b is prescribed and defined on the domain boundary $\partial\Omega$ where $\Omega \subset \mathbb{R}^2$. Note that the conservative form of the nonlinear terms is used.

Before providing some details on the spatial discretisation, we recall hereafter the time discretisation which is applied to (44) (see Section 3). For $n \geq 0$, assuming that \mathbf{u}^n , $\boldsymbol{\sigma}^n$ and p^n are known, the computation of $(\mathbf{u}^{n+1}, \boldsymbol{\sigma}^{n+1}, p^{n+1})$ consists in:

- ✓ Finding a tensor $\boldsymbol{\sigma}^{n+1}$ and an intermediate (non solenoidal) velocity $\tilde{\mathbf{u}}^{n+1}$ as solutions of:

$$(45) \quad \begin{cases} \frac{\tilde{\mathbf{u}}^{n+1} - \mathbf{u}^n}{\delta t} - \frac{1}{\mathfrak{R}e} \Delta \tilde{\mathbf{u}}^{n+1} - \frac{\mathfrak{B}i}{\mathfrak{R}e} \operatorname{div} \boldsymbol{\sigma}^{n+1} = -\nabla p^n - \operatorname{div}(\mathbf{u}^n \otimes \mathbf{u}^n), \\ \tilde{\mathbf{u}}^{n+1}|_{\partial\Omega} = \mathbf{u}_b, \\ \boldsymbol{\sigma}^{n+1} = \mathbb{P}(\boldsymbol{\sigma}^{n+1} + r \operatorname{D}\tilde{\mathbf{u}}^{n+1} + \theta(\boldsymbol{\sigma}^n - \boldsymbol{\sigma}^{n+1})). \end{cases}$$

- ✓ Projecting $\tilde{\mathbf{u}}^{n+1}$ to obtain a divergence-free velocity field \mathbf{u}^{n+1} and the pressure p^{n+1} :

$$(46) \quad \begin{cases} \frac{(\mathbf{u}^{n+1} - \tilde{\mathbf{u}}^{n+1})}{\delta t} + \nabla(p^{n+1} - p^n) = \mathbf{0}, \\ \operatorname{div} \mathbf{u}^{n+1} = 0, \\ (\mathbf{u}^{n+1} - \tilde{\mathbf{u}}^{n+1}) \cdot \mathbf{n}|_{\partial\Omega} = 0. \end{cases}$$

Remark 4. In practice, (46) is solved in two steps. First, \mathbf{u}^{n+1} is eliminated from the first equation by using the incompressibility constraint. This leads to a linear system relating p^{n+1} to the predicted velocity field $\tilde{\mathbf{u}}^{n+1}$ and to p^n . Once the new pressure has been computed, \mathbf{u}^{n+1} is updated with the help of the first equation. Note that in order to recover an almost, i.e up to the

computer accuracy, solenoidal velocity field this procedure has to be applied at the fully discrete level, i.e. after a spatial discretisation has been applied to (46).

4.1. The spatial discretisation. We denote hereafter by (u, v) the components of the velocity field \mathbf{u} . The computational domain $\Omega = (0, L_x) \times (0, L_y)$ is discretised by using a Cartesian uniform mesh. Let N_x and N_y be the number of mesh cells in the x and y directions, we define the grid points by

$$\begin{aligned} x_i &= (i - 1) h_x \quad \text{for } i = 1, \dots, N_x + 1, \\ y_j &= (j - 1) h_y \quad \text{for } j = 1, \dots, N_y + 1, \end{aligned}$$

where $h_x = L_x/N_x$ and $h_y = L_y/N_y$. With the mesh points x_i and y_j , we associate the midpoints

$$\begin{aligned} x_{i+1/2} &= \frac{1}{2}(x_{i+1} + x_i) \quad \text{for } i = 1, \dots, N_x, \\ y_{j+1/2} &= \frac{1}{2}(y_{j+1} + y_j) \quad \text{for } j = 1, \dots, N_y. \end{aligned}$$

Let a computational cell $K_{ij} = (x_i, x_{i+1}) \times (y_j, y_{j+1})$. As in the classical MAC scheme for the incompressible Navier-Stokes equations (see [13]) the discrete velocity unknowns u_{ij} and v_{ij} are located at the midpoint of the cell edges, that is $u_{ij} \approx u(x_i, y_{j+1/2})$ and $v_{ij} \approx v(x_{i+1/2}, y_j)$. The discrete pressure p_{ij} is placed at the centre of the mesh cell K_{ij} , namely $p_{ij} \approx p(x_{i+1/2}, y_{j+1/2})$. Also, the discrete components of the tensor $\boldsymbol{\sigma}$ are put all together at the centre of the mesh cell. This choice, which is an arbitrary one, allows to update all tensor components, through the local relation (12), at the same mesh locations. Note that another choice has been made in [16, 17]. None of these grid placements are fully satisfactory as they both induce grid interpolations at some steps in the numerical algorithm.

Figure 1 summarises this staggered arrangement of the unknowns.

The spatial discretisation of the first equations in (45) and (46) is achieved by performing an integration over the control volume $K_{i,j+1/2} = (x_{i-1/2}, x_{i+1/2}) \times (y_j, y_{j+1})$ for the horizontal velocity component and over $K_{i+1/2,j} = (x_i, x_{i+1}) \times (y_{j-1/2}, y_{j+1/2})$ for the vertical one. The discrete incompressibility constraint is derived from the continuous one after integration over the computational meshes K_{ij} . Classical cell-centred second-order finite volume schemes are applied to discretise first and second-order partial derivatives with respect to the spatial directions.

Boundary conditions. Additional mesh points are added outside of the computational domain, namely:

$$x_{1/2} = x_1 - \frac{h_x}{2}, \quad x_{N_x+3/2} = x_{N_x+1} + \frac{h_x}{2},$$

and similarly for y . *Ghost* values are associated with these extra mesh points in order to enforce the boundary conditions. For instance, a Dirichlet boundary condition at $y = 0$ is approximated by introducing the additional discrete velocity values $u_{i,0}$ and by writing

$$\frac{u_{i,0} + u_{i,1}}{2} = u_b(x_i, 0).$$

A second-order approximation of the boundary condition is therefore employed. Note that Neumann boundary conditions can be handled similarly.

As the spatial discretisation of the Navier-Stokes equations on a staggered grid is well known, details are omitted in the sequel. However, we provide the discrete formulae applied to the terms in (45)-(46) depending on the tensor $\boldsymbol{\sigma}$.

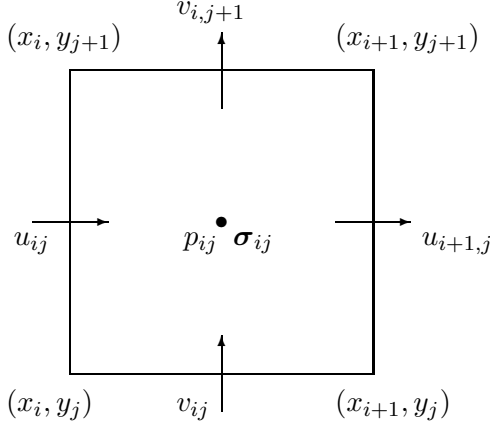


FIGURE 1. Location of the discrete unknowns in the mesh cell $K_{ij} = (x_i, x_{i+1}) \times (y_j, y_{j+1})$.

The momentum equation. For $j = 1, \dots, N_y$ and $i = 2, \dots, N_x$, the discrete contribution of the extra-stress tensor in the horizontal momentum equation writes

$$\begin{aligned}
 \int_{K_{i,j+1/2}} \operatorname{div} \boldsymbol{\sigma} \cdot \begin{pmatrix} 1 \\ 0 \end{pmatrix} d\mathbf{x} &= \int_{y_j}^{y_{j+1}} (\sigma_{11}(x_{i+1/2}, y) - \sigma_{11}(x_{i-1/2}, y)) dy \\
 &\quad + \int_{x_{i-1/2}}^{x_{i+1/2}} (\sigma_{12}(x, y_{j+1}) - \sigma_{12}(x, y_j)) dx \\
 &\approx h_y (\sigma_{11}(x_{i+1/2}, y_{j+1/2}) - \sigma_{11}(x_{i-1/2}, y_{j+1/2})) \\
 &\quad + h_x (\sigma_{12}(x_i, y_{j+1}) - \sigma_{12}(x_i, y_j)) \\
 &\approx h_y (\sigma_{11}|_{ij} - \sigma_{11}|_{i-1,j}) + h_x (\overline{\sigma_{12}}|_{i,j+1} - \overline{\sigma_{12}}|_{ij}),
 \end{aligned}$$

where $\overline{\sigma_{12}}|_{ij}$ denotes a second-order approximation of σ_{12} at the mesh point (x_i, y_j) , that is

$$\overline{\sigma_{12}}|_{ij} = \begin{cases} \frac{3}{2}(\sigma_{12}|_{i-1,1} + \sigma_{12}|_{i,1}) - \frac{1}{2}(\sigma_{12}|_{i-1,2} + \sigma_{12}|_{i,2}) & \text{for } j = 1, \\ \frac{1}{4}(\sigma_{12}|_{i-1,j-1} + \sigma_{12}|_{i-1,j} + \sigma_{12}|_{ij} + \sigma_{12}|_{i,j-1}) & \text{for } j = 2, \dots, N_y, \\ \frac{3}{2}(\sigma_{12}|_{i-1,N_y} + \sigma_{12}|_{i,N_y}) - \frac{1}{2}(\sigma_{12}|_{i,N_y-1} + \sigma_{12}|_{i-1,N_y-1}) & \text{for } j = N_y + 1. \end{cases}$$

The Bingham-projection. As the discrete velocity and the extra-stress tensor are staggered, the computation of the diagonal components of the rate-of-strain tensor $D\tilde{\mathbf{u}}^{n+1}$ in (45) is straightforward: second-order centred formulae are used. The discretisation of the off-diagonal term, involving cross partial derivatives, requires specific formulae for mesh points in the vicinity of

the domain boundary, namely for $i = 1, \dots, N_x$, we use

$$\frac{\partial u}{\partial y}(x_{i+1/2}, y_{j+1/2}) \approx \begin{cases} (3\bar{u}_{i+1/2,1/2} - 4u_b(x_{i+1/2}, 0) + \bar{u}_{i+1/2,3/2})/(3h_y) & \text{for } j = 1, \\ (\bar{u}_{i+1/2,j+3/2} - \bar{u}_{i+1/2,j-1/2})/(2h_y) & \text{for } j = 2, \dots, N_y - 1, \\ (-\bar{u}_{i+1/2,N_y-1/2} + 4u_b(x_{i+1/2}, L_y) - 3\bar{u}_{i+1/2,N_y+1/2})/(3h_y) & \text{for } j = N_y, \end{cases}$$

where $\bar{u}_{i+1/2,j+1/2}$ is the following second-order interpolation

$$\bar{u}_{i+1/2,j+1/2} = \frac{u_{ij} + u_{i,j+1}}{2}.$$

Similar formulae are employed to approximate $\frac{\partial v}{\partial x}(x_{i+1/2}, y_{j+1/2})$ which completes the discretisation of $(\mathbf{D}\tilde{\mathbf{u}}^{n+1})_{12}$.

This numerical scheme has been implemented in a F90/MPI code initially written for the simulation of Newtonian flows. The PETSc library [1, 2] is used to solve linear systems and to manage data on structured grids. The communications between the MPI processes are written explicitly by using routines of the MPI library. All the numerical simulations presented in the following sections have been performed by using p MPI processes with $4 \leq p \leq 16$.

In all numerical simulations presented below, the computational domain is $\Omega = (0, 1)^2$ and is discretised with a uniform mesh with $h_x = h_y$. We therefore denote by h the mesh size.

4.2. Code validation : numerical estimates of the convergence rates. In order to estimate the convergence rate of the numerical scheme with respect to both the spatial and temporal discretisations, we have performed simulations of a viscoplastic medium flow for $\Re = 1000$ and for $\mathfrak{B}i = 1$ in a regularised lid-driven cavity. The boundary condition is:

$$(47) \quad \mathbf{u}_b(x, y) = \begin{cases} 16(x^2(1-x)^2, 0) & \text{on the top boundary } y = 1, \\ (0, 0) & \text{elsewhere.} \end{cases}$$

Values for r and θ are set such that $r \leq \frac{1}{3\mathfrak{B}i}$ and $\theta = \delta t$. With these parameters and starting at rest, a numerical simulation has been performed up to the non-dimensional time $t = 1$ on a grid with 2048^2 mesh points and a time step $\delta t = h$, so that the CFL number is equal to unity. Let us denote by \mathbf{u}_{ref} the corresponding (discrete) velocity field. At time $t = 1$, the flow is not stationary. Indeed, the time derivatives of the velocity components are of the order of 10^{-1} in L^∞ -norm.

In order to estimate the numerical error due to the time discretisation, we have plotted on Figure 2 the L^2 -norm of the difference between \mathbf{u}_{ref} and solutions $\mathbf{u}_{\delta t}^{1024}$ computed on a grid with 1024^2 mesh points and with various increasing time steps. In order to highlight the convergence rate, logarithmic scales are used. For this particular flow configuration, we recover the expected first-order time accuracy proved in Theorem 3. On Figure 3, the L^2 -norm of the difference between \mathbf{u}_{ref} and discrete solutions \mathbf{u}_h computed on grids with mesh size h and a time step $\delta t = h$, so that the CFL number is equal to unity, is plotted for $h = 1/32, 1/64, 1/128, \dots, 1/1024$. A second-order convergence rate is found which is in agreement with the choice of the spatial discretisations used.

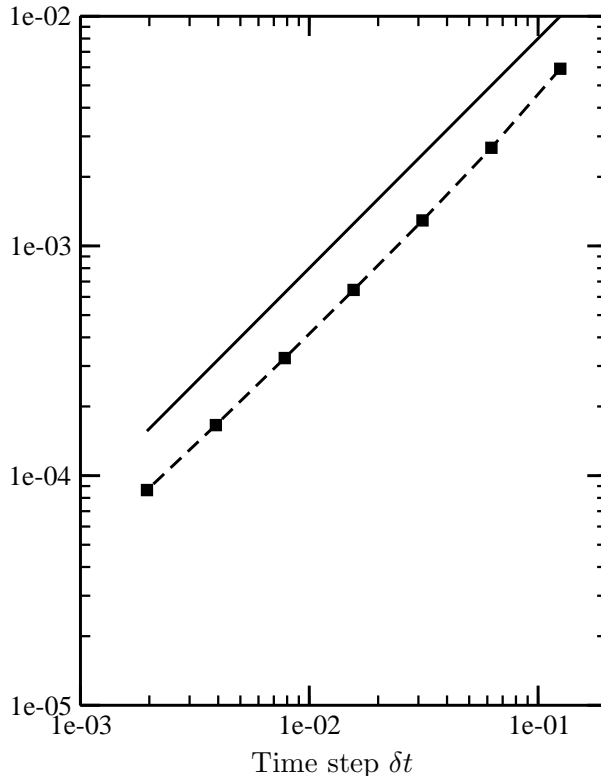


FIGURE 2. Errors $\|\mathbf{u}_{\delta t}^{1024} - \mathbf{u}_{\text{ref}}\|_2$ at time $t = 1$ plotted as a function of the time step δt . The discrete velocity fields $\mathbf{u}_{\delta t}^{1024}$ are computed on a grid with a fixed mesh size $h = 1/1024$ and time steps δt . The slope of the solid line is equal to unity.

4.3. Finite stopping times. The net effect of an external volume force and/or a nonzero Dirichlet boundary condition in the incompressible Navier-Stokes equations is to sustain the flow motion by bringing kinetic energy into the system. As it is well known, the lack of an energy source term in the case of Newtonian fluids ($\mathfrak{B}i = 0$) results in an exponential decay, with respect to time, of the L^2 -norm of the velocity field. The decay rate depends on the Reynolds number. The dynamical behaviour of viscoplastic media is completely different: when $\mathfrak{B}i \neq 0$, it can be proved that the flow motion stops in finite time (see [8] and the references therein).

In order to check if the bi-projection scheme preserves this important property of Bingham flows, we first aim to reproduce the test case used in [7] (Figure 11), namely a Bingham flow for $\mathfrak{R}e = 1$ and for $\mathfrak{B}i = \sqrt{2}$ fills a square cavity and is forced by a regularised boundary condition (47). Starting at rest, namely $\mathbf{u}_{\text{init}} = 0$, the numerical simulation is performed for times $0 < t < 0.05$ with the boundary condition (47). For $t \geq 0.05$, the time integration is pursued but the motion of the upper boundary is frozen, *i.e.* \mathbf{u}_b is set to zero. As a consequence, the flow returns to rest in finite time. On Figure 4, the time evolution of the kinetic energy, defined by

$$K(t) = \frac{1}{2} \int_{\Omega} |\mathbf{u}(\mathbf{x}, t)|^2 dx,$$

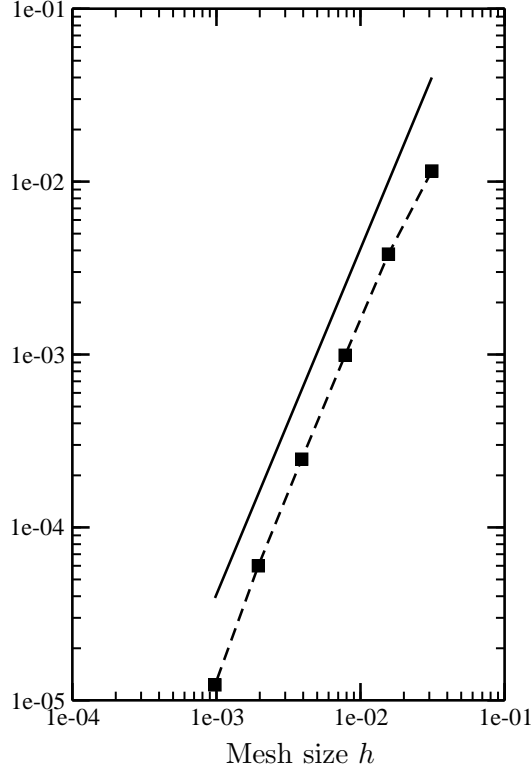


FIGURE 3. Errors $\|\mathbf{u}_h - \mathbf{u}_{\text{ref}}\|_2$ at time $t = 1$ plotted as a function of the mesh size h . The discrete velocity fields \mathbf{u}_h are computed on a grid with mesh size h . The time step δt is equal to h . Values of h are $1/1024, 1/512, 1/128, \dots, 1/32$. The slope of the solid line is equal to 2.

obtained with $\theta = 0$, which corresponds to the Uzawa-like method (see [17]), and with $\theta = \delta t$ are plotted. For both simulations, flows stop at $t \approx 0.06$, which agrees with the results shown in [7] (Figure 11) and [17].

We investigate further the cessation of Bingham flows in a lid-driven cavity for a larger Reynolds number, that is $\mathfrak{Re} = 1000$, so that the nonlinear effects are stronger which provides a more stringent numerical test cases. The boundary condition is

$$(48) \quad \mathbf{u}_b(x, y) = \begin{cases} (1, 0) & \text{on the top boundary } y = 1, \\ (0, 0) & \text{elsewhere.} \end{cases}$$

In this study, the Bingham number is successively set to $\mathfrak{Bi} = 1, 2.5, 5$ and 7.5 . The values $h = 1/256$ and $\delta t = 10^{-3}$ are respectively used for the spatial mesh and the time step. As in the previous section, the parameters r and θ are such that $r \leq \frac{1}{3\mathfrak{Bi}}$ and $\theta = \delta t$. Starting at rest, the numerical simulations are advanced in time until steady state is reached. At a stopping time t_{stop} , the energy brought into the system from the upper boundary is stopped, namely : $\mathbf{u}_b(x, y = 1, t) = 0$ for $t \geq t_{\text{stop}}$. As steady states are reached faster for larger Bingham numbers, different values for t_{stop} are used, namely $t_{\text{stop}} = 40, 35, 30$ and 25 for the respective Bingham number $\mathfrak{Bi} = 1, 2.5, 5$ and 7.5 . On Figure 5, the time evolution of the kinetic energy for these simulations is plotted. For all Bingham numbers considered, flows stop in finite time. The decay

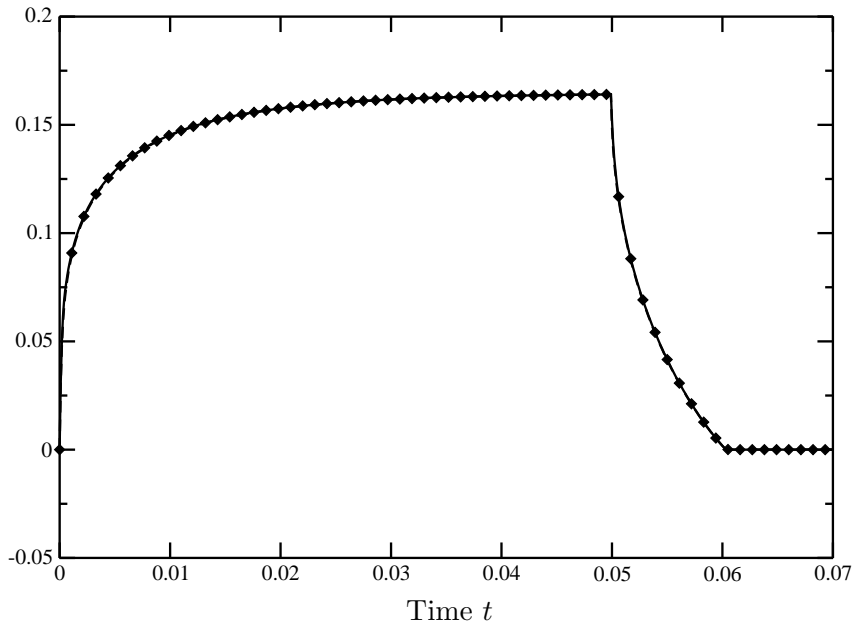


FIGURE 4. Time evolution of the kinetic energy for $\mathfrak{B}i = \sqrt{2}$ and $\mathfrak{R}e = 1$ obtained with the Uzawa-like method $\theta = 0$ (—) and with $\theta = \delta t$ (\blacklozenge). The upper boundary condition has been stopped at $t = 0.05$. The mesh size is $h = 1/64$.

of the kinetic energy during the transient period depends on $\mathfrak{B}i$. As it is expected, the flow returns to rest faster in time for larger Bingham numbers.

These numerical results show that, despite the presence of a relaxation term in the projection step used to solve the plasticity problem, the proposed bi-projection scheme is able to reproduce the cessation of Bingham flows.

4.4. Stationary flows in the lid-driven cavity for $\mathfrak{R}e = 1000$. We now focus on numerical simulations of steady flows in a lid-driven cavity: the computational domain is $\Omega = (0, 1)^2$ and the boundary conditions (48) are applied. The Reynolds number is set to $\mathfrak{R}e = 1000$. We consider that steady state is reached when the following criterion on the discrete time derivative is fulfilled

$$\frac{\|\mathbf{u}^{n+1} - \mathbf{u}^n\|_\infty}{\delta t} \leq 10^{-6}.$$

The time step is chosen so that the CFL number, defined as $\delta t \|\mathbf{u}^{n+1}\|_\infty / h$, takes values in the interval $[0.5, 1)$. In order to further validate our numerical code, we confront the reference results provided by Botella and Peyret in [4] for Newtonian fluid flows ($\mathfrak{B}i = 0$) with simulations we have performed. In Table 1, extreme values and locations of the horizontal (resp. vertical) velocity component along the vertical (resp. horizontal) centre-line are reported for mesh resolutions from 256^2 up to 1024^2 grid points. We note a very good agreement between our values and the ones listed in [4], and reported for convenience in Table 1. Moreover, by comparing the results obtained on the different meshes, the expected second-order accuracy is recovered. A perfect match is also found for the velocity profiles drawn on Figures 7 and 8.

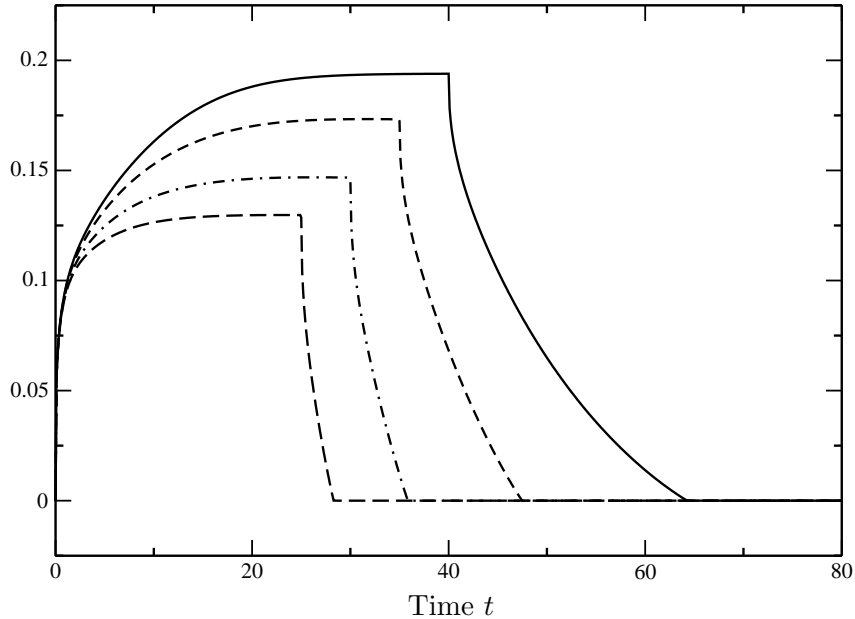


FIGURE 5. Time evolution of the kinetic energy for $\Re e = 1000$ and for $\mathfrak{B}i = 1$ (—), $\mathfrak{B}i = 2.5$ (---), $\mathfrak{B}i = 5$ (-·-·-) and $\mathfrak{B}i = 7.5$ (---). The stopping time $t_{\text{stop}} \in [25, 40]$ depends on $\mathfrak{B}i$. The spatial resolution corresponds to 256^2 mesh points.

We now reproduce some of the benchmark results proposed by Vola *et al.* in [27] of stationary viscoplastic flows for Reynolds number $\Re e = 1000$ and for Bingham numbers in the range $\mathfrak{B}i \in [1, 100]$. The fixed-point procedure (11)-(12) used to compute the plastic part $\boldsymbol{\sigma}$ of the stress tensor depends on two numerical parameters : r and θ . The former one has to fulfil the necessary condition exhibited in Theorem 3, $r \leq \frac{1}{3\mathfrak{B}i}$, and is chosen accordingly. The convergence of the fixed-point algorithm is so ensured. Its convergence rate is governed by the value of θ . Indeed, recalling the result proved in Theorem 1, the convergence of the sequence $(\boldsymbol{\sigma}^{n,k})_k$, for a fixed time iteration n , is geometric with common ratio $(1-\theta)$. This is illustrated on Figure 6. For comparison, we have drawn the convergence rate obtained with $\theta = 0$. In this particular case, the bi-projection scheme falls in the family of Uzawa-like methods (see [17]) which are known to have a slow convergence (see [7]). From Figure 6, we infer that the fixed-point algorithm can be iterated up to the desired accuracy. In practice, the Bingham projection procedure (11)-(12) is considered to be reached when the following criterion is satisfied:

$$\max_{i,j} |\boldsymbol{\sigma}_{ij}^{n,k+1} - \boldsymbol{\sigma}_{ij}^{n,k}| \leq \text{Tol},$$

where Tol is a prescribed (numerical) parameter. Values in the range $[10^{-8}; 10^{-6}]$ are used for the simulations presented in the sequel. The computational accuracy of the plastic tensor $\boldsymbol{\sigma}_{ij}^{n+1}$ clearly depends on the value of Tol. In practice, it has to be small enough so that the convergence error at this step does not affect the overall accuracy of the bi-projection scheme.

By definition, a flow is considered steady when all the time derivatives of its variables vanish. In such state, the only remaining numerical error is due to the spatial discretisation. Due to

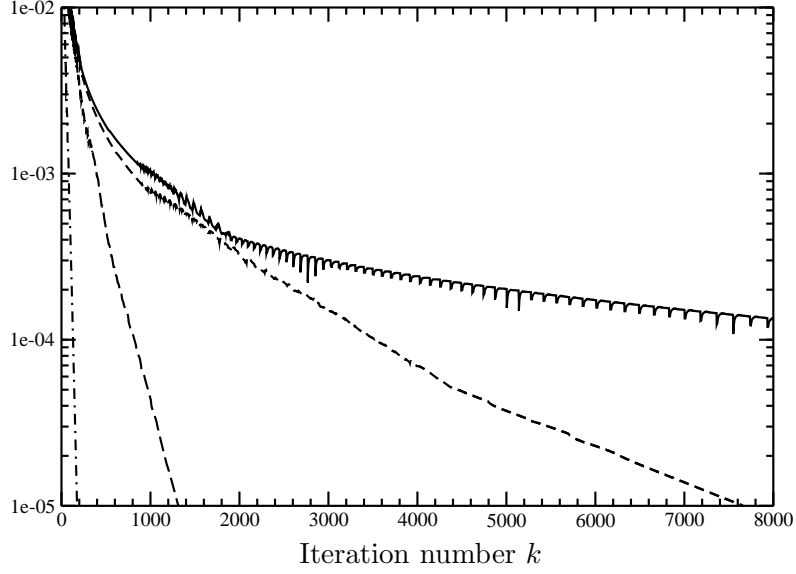


FIGURE 6. Convergence of $\|\sigma^{n,k+1} - \sigma^{n,k}\|_\infty$ with respect to the iteration number k for the Uzawa-like method $\theta = 0$ (—) and for the bi-projection scheme with $\theta = \delta t$ (---), $\theta = 10\delta t$ (-.-) and $\theta = 100\delta t$ (·-·). The numerical parameters are: $\Re e = 1000$, $\Im i = 100$, $h = 1/1024$, $\delta t = 5 \times 10^{-3}$ and $n = 200$ ($t = 0.1$). In Table 1, stationary solutions for $\Im i = 100$ were obtained with $\theta = 100\delta t$.

round-off errors and floating point arithmetic, a steady state is never reached in numerical simulations. Nevertheless, if the discrete time derivatives are small enough, the time discretisation error of the numerical scheme becomes negligible compared to the spatial one. In this peculiar situation, the time relaxation parameter θ can be set to a value much larger than the time step δt without affecting the numerical results. This ensures a faster convergence (see Figure 6) of the fixed point algorithm used to compute the plastic part of the stress tensor at each time iteration. For the numerical simulations reported in Table 1, the value $\theta = 100\delta t$ was used for the numerical simulations performed on the finest grid, namely with $h = 1/1024$ and $\delta t = 5 \times 10^{-4}$.

An overall good agreement is found for the values reported in Table 1: the differences between our results and the ones in [27] are smaller than the accuracy of the numerical scheme, that is $O(h^2)$, for $\Im i \leq 10$. For $\Im i = 10$, Vola *et al.* found that the vertical velocity along the line $y = 0.5$ has a local maximum at $x \approx 0.34$; this results was obtained on a coarse mesh with 80^2 mesh points. When refining the computational mesh, we note that the location of the local maximum moves closer to the centre of the cavity ($x \approx 0.46$). A discrepancy is also found for the values of $\min_x v(x, 0.5)$ and $\max_x v(x, 0.5)$ for the largest Bingham number $\Im i = 100$. Results in Table 1 show that, in this case, the mesh has to be fine enough: 512^2 grid points are necessary to compute the correct order of magnitude for the flow characteristics. It may seem counter-intuitive, as the net effect of the plastic tensor is to slow down the flow motion so that we may expect that coarser mesh resolutions could be used when the Bingham number is increased. Note that in [27], the numerical simulations were performed on much coarser meshes.

Finally, on Figure 9 the streamlines and the rigid zones (in practice, we use $|\mathbf{Du}| \leq 10^{-5}$), that are areas where the rate-of-strain tensor vanishes, are drawn for the different values of the Bingham number. By comparing with Figure 4 in [27], we note as previously that a good qualitative agreement is obtained. Note that Muravleva in [16] reports numerical simulations performed on a grid with 1024^2 mesh points. The time step δt is equal to 5×10^{-4} for $\mathfrak{Re} \leq 50\,000$ and 2.5×10^{-4} otherwise. As in the previous section, the time-relaxation parameter θ , used in the plastic projection step, was chosen of the order of $100\delta t$. On Figure 10, streamlines and unyielded zones ($|\mathbf{Du}| \leq 10^{-4}$) are shown for various Reynolds numbers up to 200 000. In agreement with the results reported in [16, 25] (for the most recent ones on the subject), two rigid zones are found for Reynolds numbers $\mathfrak{Re} \leq 5\,000$. A large unyielded zone fills the bottom of the cavity so that the motion of the viscoplastic material only occurs in a small region just under the top boundary. This motionless part of the flow is pushed towards the bottom of the cavity when the Reynolds number is increased, leaving more and more space for the material to move. For $\mathfrak{Re} \geq 100\,000$, it splits into two zones stuck to the wall in the lower

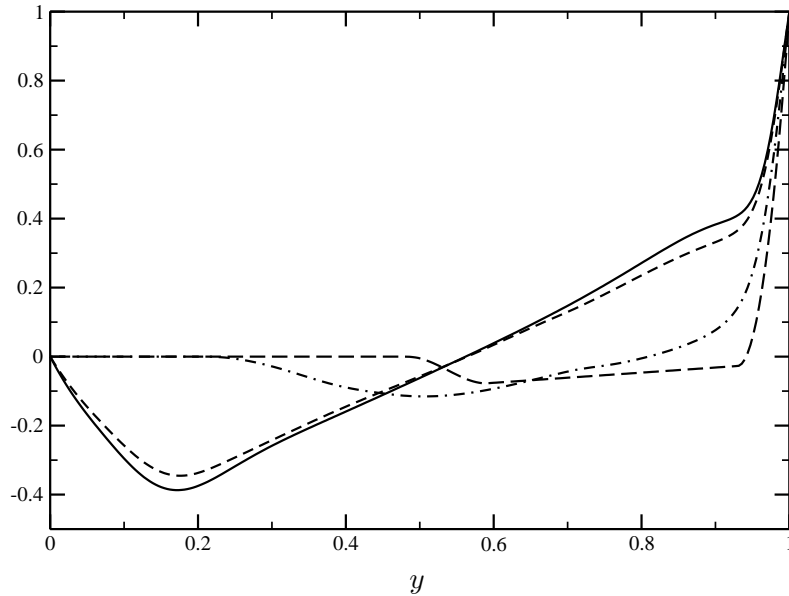


FIGURE 7. Horizontal velocity profiles along the centre-line $x = 0.5$ for stationary solutions for $\mathfrak{Re} = 1\,000$ and for $\mathfrak{Bi} = 0$ (—), $\mathfrak{Bi} = 1$ (---), $\mathfrak{Bi} = 10$ (-·-·-) and $\mathfrak{Bi} = 100$ (- - -).

4.5. Effect of the Reynolds number on Bingham flows for $\mathfrak{Bi} = 100$. In this last section, we investigate the effect of the Reynolds number on the flow motion for a fixed Bingham number $\mathfrak{Bi} = 100$. The Reynolds number is increased from $\mathfrak{Re} = 1\,000$ up to $\mathfrak{Re} = 200\,000$. For larger values steady states could not be reached and a non-stationary solution was obtained for $\mathfrak{Re} = 500\,000$. The study of unsteady Bingham flows in a lid-driven cavity is challenging and of interest but is beyond the scope of this paper. All numerical simulations reported in this section were performed on a grid with 1024^2 mesh points. The time step δt is equal to 5×10^{-4} for $\mathfrak{Re} \leq 50\,000$ and 2.5×10^{-4} otherwise. As in the previous section, the time-relaxation parameter θ , used in the plastic projection step, was chosen of the order of $100\delta t$. On Figure 10, streamlines and unyielded zones ($|\mathbf{Du}| \leq 10^{-4}$) are shown for various Reynolds numbers up to 200 000. In agreement with the results reported in [16, 25] (for the most recent ones on the subject), two rigid zones are found for Reynolds numbers $\mathfrak{Re} \leq 5\,000$. A large unyielded zone fills the bottom of the cavity so that the motion of the viscoplastic material only occurs in a small region just under the top boundary. This motionless part of the flow is pushed towards the bottom of the cavity when the Reynolds number is increased, leaving more and more space for the material to move. For $\mathfrak{Re} \geq 100\,000$, it splits into two zones stuck to the wall in the lower

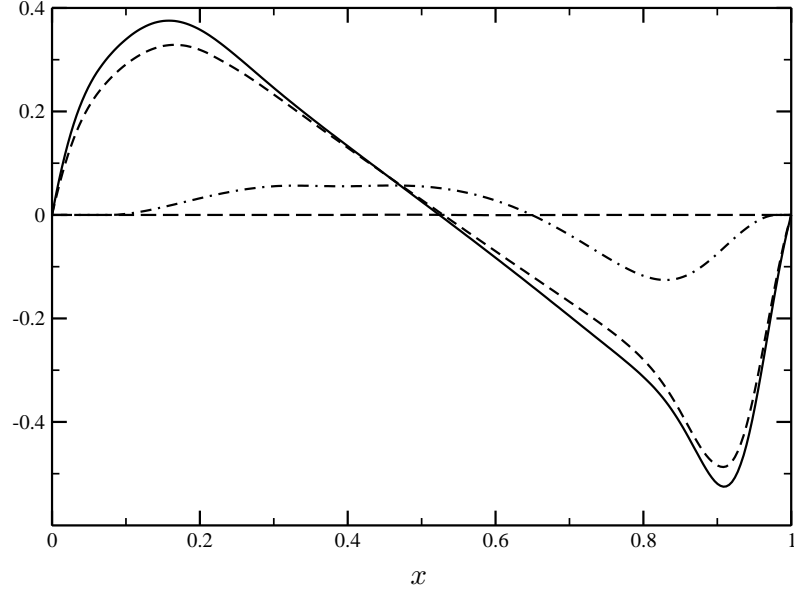


FIGURE 8. Vertical velocity profiles along the centre-line $y = 0.5$ for stationary solutions for $\Re e = 1000$ and for $\mathfrak{B}i = 0$ (—), $\mathfrak{B}i = 1$ (---), $\mathfrak{B}i = 10$ (-·-·-) and $\mathfrak{B}i = 100$ (- - -).

TABLE 1. Extreme values of the velocity along the centre-lines $x = 0.5$ and $y = 0.5$ for stationary solutions for $\Re e = 1000$ and for $\mathfrak{B}i$ in the range $[0, 100]$.

$\mathfrak{B}i$	Mesh	y_{\min}	$\min_y u(0.5, y)$	x_{\min}	$\min_x v(x, 0.5)$	x_{\max}	$\max_x v(x, 0.5)$
0	256^2	0.17383	-0.38700	0.90820	-0.52514	0.16211	0.37533
	512^2	0.17188	-0.38817	0.90918	-0.52661	0.15723	0.37658
	1024^2	0.17139	-0.38847	0.90967	-0.52694	0.15771	0.37685
	Ref. [4]	0.1717	-0.3886	0.9092	-0.5271	0.1578	0.3769
1	256^2	0.17773	-0.34533	0.90820	-0.48717	0.16602	0.32871
	512^2	0.17578	-0.34651	0.90723	-0.48856	0.16601	0.32981
	1024^2	0.17578	-0.34680	0.90771	-0.48892	0.16602	0.33009
	Ref. [27]	0.175	-0.3438	0.9	-0.482	0.1625	0.3286
10	256^2	0.50586	-0.11533	0.83008	-0.12577	0.46094	0.05689
	512^2	0.50488	-0.11628	0.83008	-0.12764	0.46094	0.05791
	1024^2	0.50439	-0.11652	0.83057	-0.12811	0.46045	0.05817
	Ref. [27]	0.5	-0.1156	0.825	-0.1258	0.3375	0.0572
100	256^2	0.58789	-0.0775	0.60742	-0.000438	0.47070	0.000432
	512^2	0.59082	-0.0777	0.60254	-0.000325	0.47754	0.000321
	1024^2	0.59131	-0.0777	0.60156	-0.000301	0.47852	0.000297
	Ref. [27]	0.6	-0.0762	0.6125	-0.0002	0.4625	0.00017

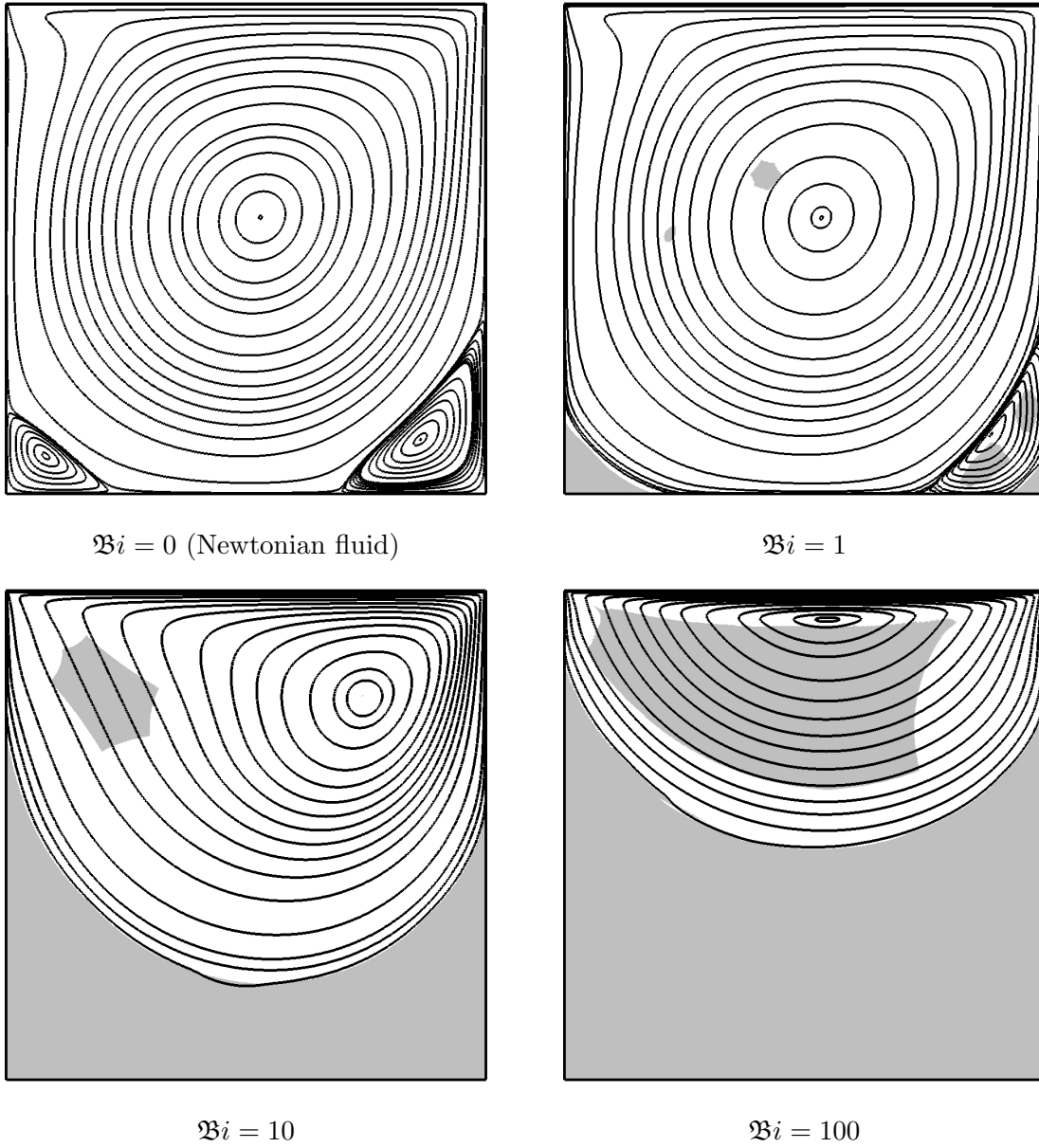


FIGURE 9. Streamlines and rigid zones ($|\mathbf{Du}| \leq 10^{-5}$) for $\mathfrak{Re} = 1000$ and for various Bingham numbers $\mathfrak{B}i$. The spatial resolution is 1024^2 , the time step is $\delta t = 5 \times 10^{-4}$ and $\theta = 0.05$.

corners. A small unyielded zone, located inside the vortex which is centred just below the lid for $\mathfrak{Re} = 1000$, appears for Reynolds numbers $\mathfrak{Re} \geq 10\,000$. This zone expands for $\mathfrak{Re} \leq 10\,000$ and starts to shrink when the Reynolds number is increased up to the largest value ($\mathfrak{Re} = 200\,000$) considered here. An unyielded zone of small size and located near the vortex centre appears

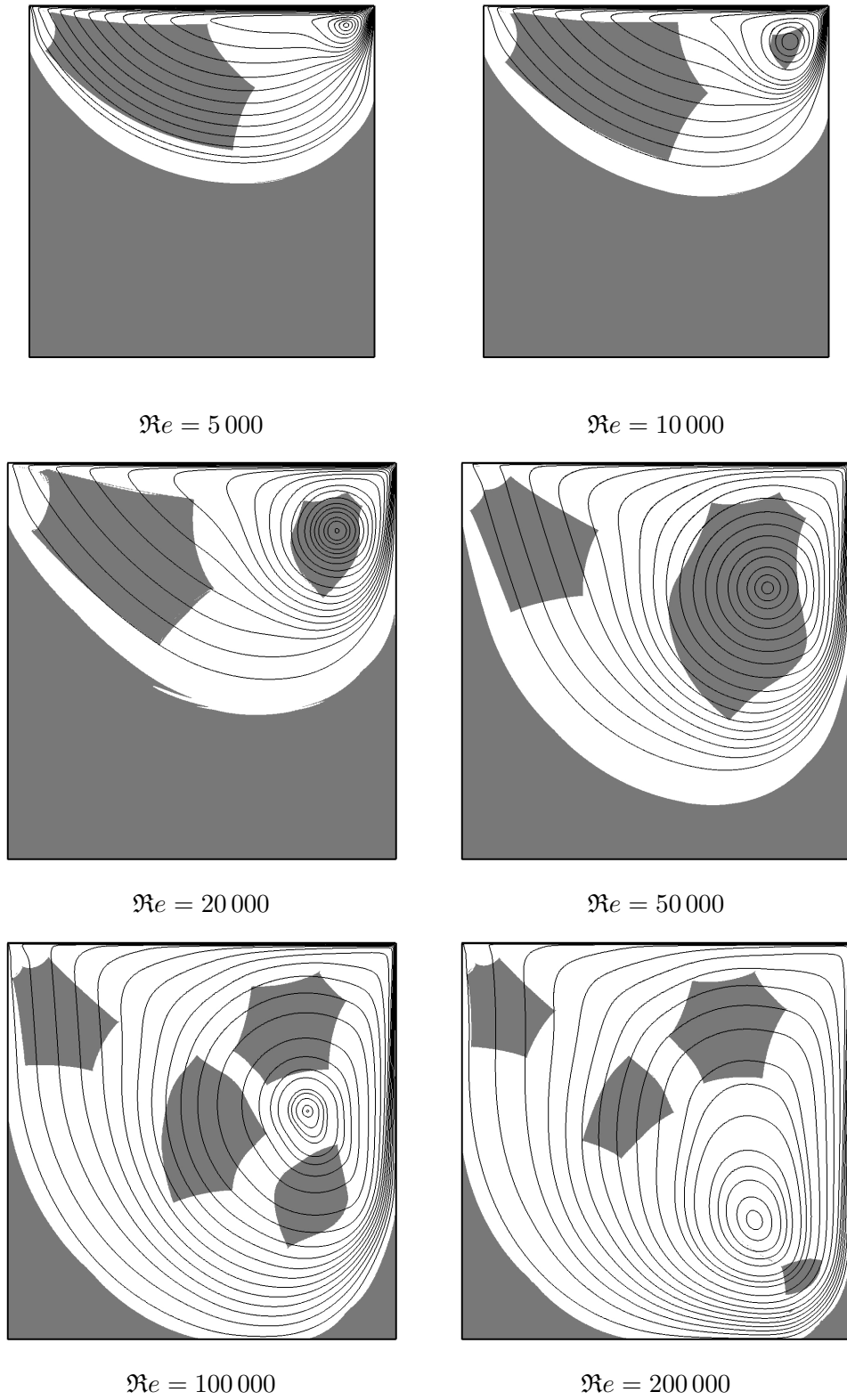


FIGURE 10. Streamlines and rigid zones ($|\mathbf{Du}| \leq 10^{-4}$) for $\mathfrak{B}i = 100$ and for increasing Reynolds numbers $\Re e$. The numerical parameters are: $h = 1/1024$, $\delta t = 5 \times 10^{-4}$ and $\theta = 5 \times 10^{-2}$.

for $\Re = 10\,000$, then expands for \Re up to $50\,000$, before to break down in several parts for $\Re \geq 100\,000$ remaining in the neighbourhood of the vortex centre.

As it has been observed in [16, 25], for $\Re \in [1\,000, 10\,000]$ the vortex is shifted towards the right corner at the top of the cavity. For larger values of the Reynolds number, $\Re \leq 20\,000$, the vortex moves towards the centre of the cavity and away from the lid. For $\Re \geq 20\,000$, the vortex centre moves towards the bottom of the cavity, remaining in a narrow vertical region defined by $[0.75, 0.85] \times [0.3, 0.83]$. As the vortex moves away from the lid, acting as an energy sink, its strength decreases.

In summary, the effect on the flow of increasing the Reynolds number is to multiply the number of unyielded zones while diminishing their sizes. As a consequence, more and more space is left for the material to move so that we may expect to finally find non-stationary solutions with non-trivial dynamics. Such study will be addressed in future works.

5. CONCLUDING REMARKS

A new numerical scheme has been proposed for the time discretisation of a system of equations modelling the isothermal and unsteady flow of an incompressible viscoplastic Bingham medium. The non-differentiable definition of the plastic part of the stress tensor is rewritten by introducing a projection operator. The flow is therefore subject to two constraints: the classical one due to the incompressibility assumption and the second one related to the plastic (yield) stress tensor. The time discretisation is based on a first-order projection scheme in its incremental version. Schematically, projection schemes consist in two steps. The former predicts a non-solenoidal velocity field by solving an advection-diffusion equation. The latter is a projection onto the space of divergence-free velocity fields. It provides a pressure, solution of a Poisson-like equation, which is then used to correct the predicted velocity. In terms of arithmetic operations, this step is the most consuming one.

The yield stress tensor is treated implicitly and is added into the prediction step. It is computed with the help of a fixed-point algorithm. Such numerical procedure, similar to the Uzawa-like method for solving Bingham flows, is known to converge slowly. In order to increase the convergence rate of the plasticity step of the numerical scheme, a pseudo-time relaxation term is added into the projection operator used to compute the yield stress tensor. As a result, the fixed-point algorithm converges geometrically with a common ratio depending on a prescribed numerical parameter. This is a key feature of the proposed bi-projection scheme providing a reasonably fast computation of the plastic stress tensor. Like numerical schemes based on a variational inequality formulation of the Bingham model, namely Uzawa-like and augmented Lagrangian methods, the bi-projection scheme has the intrinsic capability of accurately capturing the unyielded zones. Also, to implement the bi-projection scheme in an existing solver, using a projection scheme, is straightforward: the Bingham projection only requires local computations (on the computational mesh) of the plastic stress tensor.

The first part of the paper is devoted to stability and error analyses of the numerical scheme which is shown to be first-order in time. In a second part, several numerical simulations are performed. The scheme is assessed against previous published benchmark results for both Newtonian and Bingham flows in a lid-driven cavity for Reynolds number $1\,000$ and for various Bingham numbers from 1 up to 100 . The dependency of the computed solutions on the mesh resolution is investigated. For large values of the Bingham number, we observe that the computational grid has to be fine enough in order to properly compute both the fluid and rigid zones

characterising Bingham viscoplastic flows. Also, the proposed numerical scheme is shown to be able to reproduce the cessation in finite time of a viscoplastic medium in the absence of energy source terms in the equations. Finally, in order to show the capability of the proposed scheme to compute viscoplastic flows at large Bingham and Reynolds numbers, we provide results of simulations performed with the value $\mathfrak{B}i = 100$ and for various $\mathfrak{R}e$ from 1000 up to 200000. The effect of the Reynolds number on the flow behaviour is discussed.

While the proposed numerical scheme applies to a time dependent problem, only convergence to steady state solutions are presented in this paper. As a preliminary result, not shown in the present work, a non-stationary flow has been obtained for $\mathfrak{R}e = 500000$. A detailed study of unsteady solutions is feasible but is out of the scope of this paper. This will be addressed elsewhere. In order to further demonstrate the efficiency of the bi-projection method proposed and analysed in this paper, another challenging future work would be to apply the numerical scheme to the numerical simulation of three-dimensional flows. Again, this is postponed to future publications.

ACKNOWLEDGEMENTS

This research was partially supported by the French Government Laboratory of Excellence initiative n° ANR-10-LABX-0006, the Région Auvergne and the European Regional Development Fund. This is Laboratory of Excellence ClerVolc contribution number 132. The numerical simulations have been performed on a DELL cluster with 32 processors Xeon E2650v2 (8 cores), 1 To of total memory and an infiniband (FDR 56Gb/s) connecting network.

REFERENCES

- [1] S. Balay, S. Abhyankar, M. F. Adams, J. Brown, P. Brune, K. Buschelman, V. Eijkhout, W. D. Gropp, D. Kaushik, M. G. Knepley, L. Curfman McInnes, K. Rupp, B. F. Smith and H. Zhang, *PETSc Web page*, <http://www.mcs.anl.gov/petsc>, 2014.
- [2] S. Balay, S. Abhyankar, M. F. Adams, J. Brown, P. Brune, K. Buschelman, V. Eijkhout, W. D. Gropp, D. Kaushik, M. G. Knepley, L. Curfman McInnes, K. Rupp, B. F. Smith and H. Zhang, *PETSc Users Manual*, Argonne National Laboratory, ANL-95/11 - Revision 3.5, 2014.
- [3] M. Bercovier and M. Engelman. A finite element method for incompressible non-Newtonian flows. *J. Comp. Phys.* **36**(3), 313-326, 1980.
- [4] O. Botella and R. Peyret, Benchmark spectral results on the lid-driven cavity flow, *Comp. Fluids* **27** (4), 421–433, 1998.
- [5] M. Chatzimina, G.C. Georgiou, I. Argyropaidas, E. Mitsoulis and R.R. Huilgol, Cessation of Couette and Poiseuille flows of a Bingham plastic and finite stopping times, *J. Non-Newtonian Fluid Mech.*, **129**, 117-127, 2005.
- [6] E.J. Dean, R. Glowinski, Operator-splitting methods for the simulation of Bingham visco-plastic flow, *Chin. Ann. Math.*, **B23**, 187-204, 2002.
- [7] E.J. Dean, R. Glowinski and G. Guidoboni, On the numerical simulation of Bingham viscoplastic flow: old and new results. *J. Non-Newtonian Fluid Mech.*, **142**, 36–62, 2007.
- [8] J.I. Diaz, R. Glowinski, G. Guidoboni and T. Kim, Qualitative properties and approximation of solutions of Bingham flows: on the stabilization for large time and the geometry of the support. *Revista de la Real Academia de Ciencias, serie A: Mathematicas*, **104** (1), 2010.
- [9] G. Duvaut and J.- L. Lions, Les Inéquations en Mécanique et en Physique. *Dunod*, 1972.
- [10] M. Fortin and R. Glowinski, Augmented Lagrangian Methods : Applications to the Numerical Solutions of Boundary-Value Problems, *North-Holland*, Amsterdam, 1983.
- [11] R. Glowinski, J.L. Lions and Tremolieres, Numerical Analysis of Variational Inequalities, *North-Holland*, Amsterdam, 1981.

- [12] J.-L. Guermond, P. Mineev and J. Shen, An Overview of Projection methods for incompressible flows. *Comp. Meth. Appl. Mech. Engng.*, **195**, 6011-6045, 2006.
- [13] F.H. Harlow and J.E. Welch, Numerical calculation of time-dependent viscous incompressible flow of fluid with free surface. *Phys. Fluids*, **12**(8), 2182-2189, 1965.
- [14] E. Mitsoulis, Flows of viscoplastic materials: models and computations, *Rheology Reviews*, 135-178, 2007.
- [15] E. Mitsoulis and Th. Zisis, Flow of Bingham plastics in a lid-driven square cavity, *J. Non-Newtonian Fluid Mech.* **101**, 173-180, 2001.
- [16] L. Muravleva, Uzawa-like methods for numerical modelling of unsteady viscoplastic Bingham medium flows, *Applied Numerical Mathematics*, <http://dx.doi.org/10.1016/j.apnum.2014.06.001>, 2014.
- [17] L.V. Muravleva and E.A. Muravleva, Uzawa method on semi-staggered grids for unsteady Bingham media flows. *Russ. J. Numer. Math. Modelling*, **24**(6), 543-563, 2009.
- [18] E.A. Muravleva and M.A. Olshanskii, Two finite-difference schemes for calculation of Bingham fluid flows in a cavity. *Russ. J. Numer. Anal. Math. Modelling* **23**(6), 615-634, 2008.
- [19] M.A. Olshanskii, Analysis of semi-staggered finite-difference method with application to Bingham flows. *Comp. Meth. Appl. Mech. Engng.*, **198**, 975-985, 2009.
- [20] T.C. Papanastasiou, Flows of materials with yield. *J. Rheol.* **31**(5), 385-404, 1987.
- [21] N. Roquet and P. Saramito, An adaptive finite element method for Bingham fluid flows around a cylinder. *Comput. Methods Appl. Mech. Engng.* **192**, 3317-3341, 2003.
- [22] F.J. Sanchez, Application of a first-order operator splitting method to Bingham fluid flow simulation, *Comput. Math. Appl.*, **36**(3), 71-86, 1998.
- [23] J. Shen, On error estimates of the projection methods for the Navier-Stokes equations: first-order schemes. *SIAM J. Numer. Anal.*, **29**, 55-77, 1992.
- [24] J. Shen, Remarks on pressure error estimates of the projection methods. *Numer. Math.*, **67**, 513-520, 1994.
- [25] A. Syrakos, G.C. Georgiou and A.N. Alexandrou, Performance of the finite volume method in solving regularised Bingham flows: Inertia effects in the lid-driven cavity flow. *J. Non-Newtonian Fluid Mech.*, **208-209**, 88-107, 2014.
- [26] R. Temam, Navier-Stokes Equations. Theory and Numerical Analysis. *North-Holland, Amsterdam*, 1984.
- [27] D. Vola, L. Boscardin and J.C. Latché, Laminar unsteady flows of Bingham fluids: a numerical strategy and some benchmark results. *J. Comput. Phys.*, **187**, 441-456, 2003.
- [28] Y. Zhang, Error estimates for the numerical approximation of time-dependent flow of Bingham fluid in cylindrical pipes by the regularization method, *Numer. Math.* **96**(1), 153-184, 2003.

LABORATOIRE DE MATHÉMATIQUES UMR 6620, UNIVERSITÉ BLAISE PASCAL, CAMPUS DES CÉZEAUX - B.P. 80026, 63171 AUBIÈRE CEDEX, FRANCE

E-mail address: Laurent.Chupin@math.univ-bpclermont.fr; Thierry.Dubois@math.univ-bpclermont.fr